3

Chapter

Mechanical design of induction machine rotor

The iterative design procedure required for the development of a high speed active magnetic bearing (AMB) supported induction machine (IM) rotor is described. The chapter is divided into conceptual and preliminary design sections, where the design tools are developed for the detail mechanical design of rotor section. During the development of the design tools, the analytical calculations are verified using finite element analysis (FEA) and the simulations are validated through strain gage measurements. The detail mechanical design which includes material selection, rotor configuration-optimization and detail stress analysis is then discussed. The chapter is concluded with an overview of the process followed and some of the assumptions made to formulate the optimum solution.

3.1 Iterative design process

Due to the complexity of a high speed drive design, an iterative design process is required for the solution to fulfil all the design requirements. Figure 3-1 gives an overview of the process to be followed during the development of a high speed rotor, with emphasis on the mechanical aspects. The development process includes conceptual, preliminary and detail designs and is concluded with the production phase.

The process begins with a drive specification, derived from the drive application. From the drive specifications the conceptual design can begin and includes selecting the machine and bearing topology, followed by a conceptual layout of the system. The preliminary design includes rough sizing of the machine and bearings considering both electrical and mechanical parameters. Preliminary material selection is followed by the calculation of the maximum allowable rotor outer diameter (OD) as well as calculating the required interference for the magnetic core/shaft shrink fit. The designs have to conform to certain electromagnetic and mechanical requirements before the detail design phase can commence.

Detail design includes detail mechanical and electromagnetic design of both the electric motor and choice of bearings. The rotor mechanical design includes material selection, calculating final required interference and detailed stress and rotor dynamic analyses. The detail designs will have to conform to certain electromagnetic and mechanical requirements before the production phase which includes manufacturing, assembly and commissioning of the product can commence.

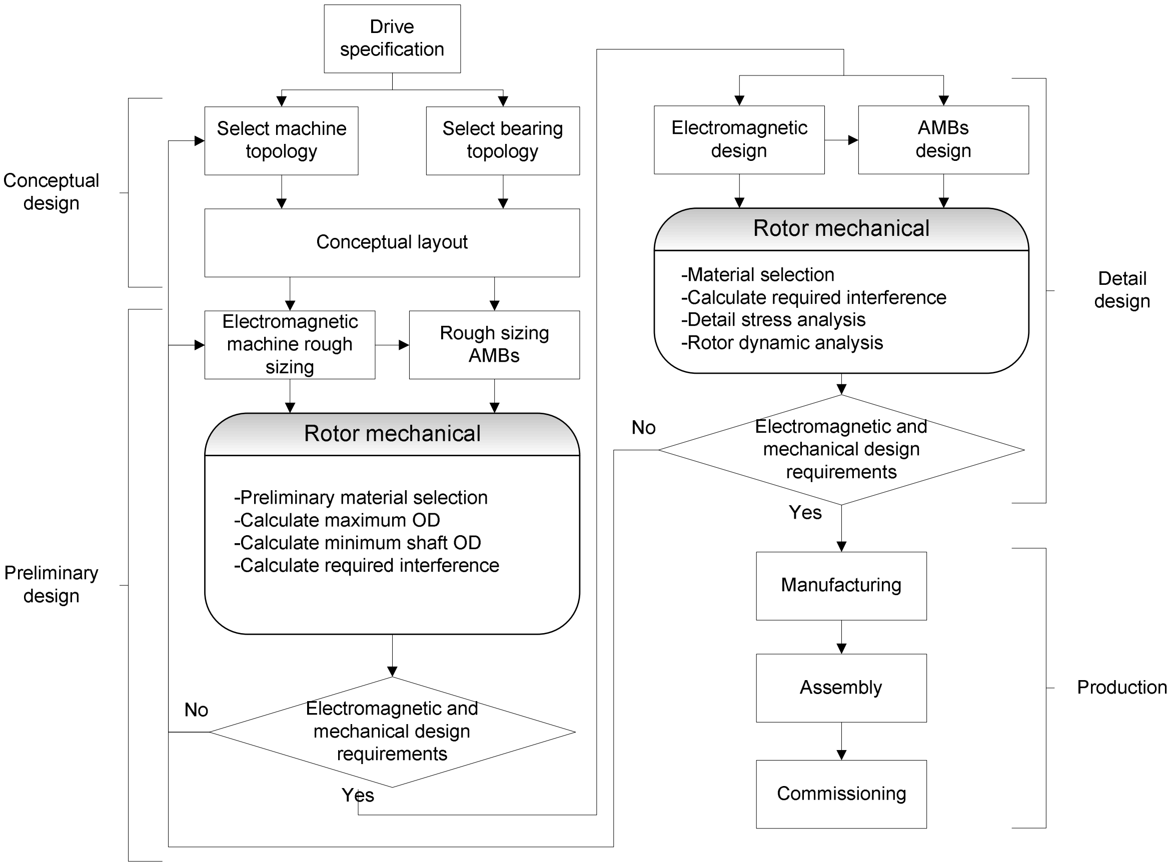

Figure 3-1: Schematic illustration of the iterative design process

After establishing the high level process to follow during the development of a high speed drive, the process can now be implemented. This is done throughout the remainder of the chapter with the focus on the mechanical design of the IM rotor section.

3.2 Drive specifications

From the iterative design process it is apparent that the drive specifications are required. The drive is designed for a blower application, used to circulate the coolant in a high temperature reactor. The first step would be to formulate the blower specifications, from which the drive specifications can be derived. The resulting drive specification for this application is given in Table 3-1. The specification includes the maximum operating speed and temperature of the rotor and the required machine power. Due to the nature of the application, one design requirement is that no lubrication can be used due to the risk of contamination. Consequently, no mechanical contact is allowed. The design also requires an interface to couple the blower impeller directly onto the rotor, thus eliminating the use of a gearbox or belt drive. The direct drive is only possible due to the implementation of a variable speed drive. The design also requires a relative conservative mechanical factor of safety (FOS), due to the nature of the application and this being a first iteration research project.

Table 3-1: Drive specifications

Parameter	Specification	Description/comment
Maximum operating speed N_{max}	25,500 r/min	Maximum operating speed with an over speed of 27,000 r/min
Ambient operating temperature T	80 °C	All temperature affected calculations are done with the assumption that the components are at an ambient temperature
Machine power	100 kW	The mechanical power required is derived from the blower specifications
No mechanical contact	N/A	Due to the application no lubrication can be used, as it will contaminate the coolant
Blower impeller interface	N/A	With the exclusion of a gearbox the blower can be attached directly to the machine shaft
Mechanical FOS	2	The Von Mises equivalent stress should be smaller or equal to half the material's yield strength

3.3 Conceptual design

After establishing the drive specifications the conceptual design phase follows. During the conceptual design the machine and bearing topology is selected. The induction machine (IM) is the preferred machine for this application due to the experience of the research group, the operating conditions and the relative low cost compared to a permanent magnet synchronous machine (PMSM). Active magnetic bearings (AMBs) are also the preferred bearings for the application due to the no lubrication requirement and the design capability of the research group.

After the selection of the machine and bearing topology a conceptual layout as illustrated in Figure 3-2 is required. The motor and AMB design engineers are responsible for the conceptual machine layout and rough sizing of the motor and AMB's after which the preliminary design phase can begin. Although the sections to follow involve both mechanical and electrical aspects, the focus will be on the mechanical design.

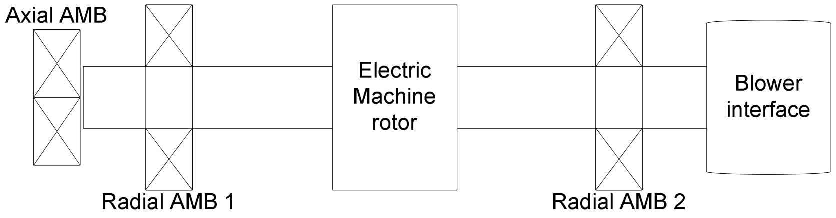

Figure 3-2: Drive conceptual layout

3.4 Preliminary mechanical design

After the rough sizing of the machine, both electrical and mechanical calculations are required in order to start the optimization process. The induction machine's size (volume) can be reduced with an increase in operating speed, without lowering the power delivery. However, an increase in speed enhances the mechanical design challenges.

A good starting point for the mechanical design, when the operating speed is known, is calculating the maximum OD of the rotor. Jussi Lähteenmäki [11] gives basic equations that can be used for calculating the maximum outer diameter $D_{r,}$ surface speed v_c and a the first critical speed ω_c for a laminated rotor using (3.1), (3.2) and (3.3). The required variables are σ_{max} maximum allowable stress in the lamination material, ρ the material density, υ poison ratio, E the modulus of elasticity, d_r the ID of the laminations, l the distance between the bearings and n is the rotating speed in revolutions per second. Figure 3-3 illustrates the basic components for a laminated cage rotor and also indicates the laminations ID and rotor OD.

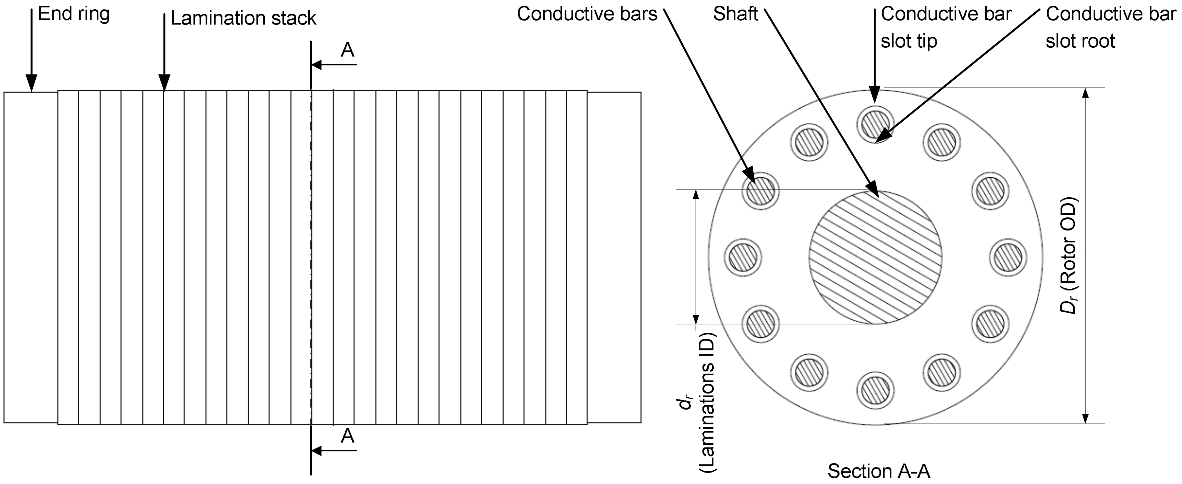

Figure 3-3: Induction machine illustration

$$D_r \leq \sqrt{\frac{4\sigma_{\max}}{\rho\pi^2 n^2 (3+\upsilon)} - \frac{(1-\upsilon)}{(3+\upsilon)} d_r^{\ 2}} \tag{3.1}$$

$$v_c = \pi D_r n \leq \sqrt{\frac{4\sigma_{\max}}{\rho\left[(1-\upsilon)\left(\frac{d_r}{D_r}\right)^2 + (3+\upsilon)\right]}} \tag{3.2}$$

$$\omega_c = \sqrt{\left(\frac{d_r}{D_r}\right)^4 \frac{3ED_r^{\ 2}}{\rho l^4}} \tag{3.3}$$

Although these equations are used to calculate the maximum rotor diameter after preliminary material selection, it will not be the case in this instance. Due to the project being a first iteration research project and due to time constraints the rotor dimensions were included in the design specifications as shown in Table 3-2. Consequently the equations are used to calculate the minimum required material strength for the specific geometry and operating conditions.

Table 3-2: Geometry specifications

Parameter	Specification	Description/comment
Shaft OD	80 mm	The shaft OD is determined by the rotordynamic analysis.
Rotor core OD	123 mm	The rotor core OD is determined by the stator ID
Rotor core axial length	177 mm	The rotor core length is determined by the electromagnetic and rotor dynamic design
Number of conductive bars	24	The number of bars making up the cage is determined by the electromagnetic design and geometrical layout.
Conductive bar diameter	10 mm	Round conductive bars are used to minimize stress concentrations

From (3.1) it is found that a rotor with operating speed of 27,000 r/min, laminations inner diameter d_r = 80 mm and rotor outer diameter D_r = 123 mm ($v_c \approx$ 174 m/s) the maximum stress is 218 MPa. However, Lähteenmäki suggests that for a cage rotor the speed should be decreased by about 17% ($v_c \approx$ 144 m/s ≈ 22,350 r/min). This is due to the fact that the lamination material should contain the cage as well as support itself. However, the modification factor is found to be a rough estimation, especially if it is considered how a change in the cage material's density will influence the maximum stress. During the detail stress analysis it will be shown that for a limiting stress of 218 MPa and a diameter of 123 mm, 22,350 r/min is overly ambitious. It is mainly due to the stress concentration produced by the bar slots that a stress concentration factor should be included into these equations. From the experience gained by the detail design it is the author's opinion that a 30% reduction in operating speed is better suited for a cage rotor. The percentage can vary depending on the bar slot geometry and position. Furthermore the 30% compensation factor is for aluminium bars and will become even more if copper bars are used.

With the maximum stress in the laminated core calculated, some preliminary end ring stress calculations can be done. It will be shown that the choice of end ring material is not only an electromagnetic choice but also influenced by the material strength. To illustrate this, consider a rotor operating at 27,000 r/min with an end ring inner diameter of 80 mm and an outer diameter of 123 mm. Using (3.1) with no compensation factor, an aluminium alloy end ring will have a maximum stress of 74 MPa. However, a copper alloy end ring will have a maximum stress of about 240 MPa. Using a FOS of 2, the yield strength of the aluminium required is 148 MPa, while the copper requires a yield strength of about 480 MPa. From these initial calculations it is shown that a high strength copper alloy will is needed to adhere to the strength requirements.

Equation (3.3) is used to calculate the first critical speed of the shaft, however, it is found to be an inconclusive calculation. It will be extremely difficult to find a simple equation that calculates the critical frequencies accurately, mainly due to the wide range of rotor geometry possibilities. Factors not included into this equation and that will have a significant influence are bearing stiffness and mass not contributing to the shaft stiffness. However, although (3.3) is inconclusive, it will be a useful first order value to have a feel for the rotordynamic stability of a rotor. Although the rotor dynamics of the rotor is mentioned here, the detail analysis is done as part of the rotor delevitation design [**8**]. The analysis does however have an influence on the final dimensions and operating speed.

3.4.1 Preliminary interference calculations

With the shrink fit as the selected core/shaft connection, the amount of interference required is a critical calculation. From the literature Larsonneur's [3] derivation for calculating the stress in two shrink fitted rotating rings, can be implemented. Figure 3-4 illustrates the stress distribution in the ring and shaft. The three graphs represents the radial, tangential and the combined stress in each component. The preliminary calculations indicate the minimum interference required to ensure there is no loss in contact between the hub and shaft. MATLAB® is used for the calculations and the source code is included in Appendix A. Although the derivation is based on planar stress (stress in thin discs) and no geometry irregularities, which is possibly not the case, the results provide a good initial value for the interference required.

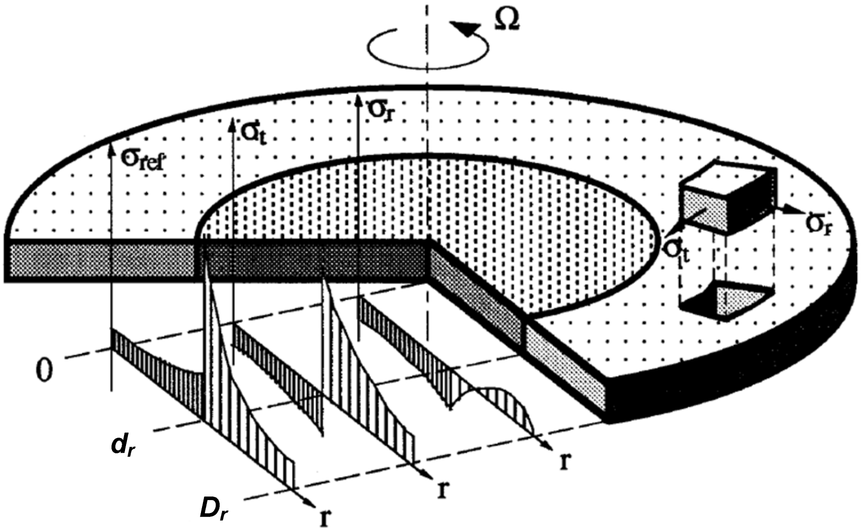

Figure 3-4: Illustration of the stress distribution for a shrink fitted solid ring onto a solid shaft [3]

In order to illustrate some results from the MATLAB® simulation, Figure 3-5 to Figure 3-8 are included. This particular simulation is for illustrative purposes only, with typical mild steel material properties and a solid shaft OD = 80 mm, ring OD 123 mm and a 90 µm interference rotating at 27 000 r/min. Figure 3-5 shows the radial stress calculated in both the shaft and solid outer ring. The x-axis indicates the radial position where the stress is calculated and the y-axis is the magnitude of the stress. The sudden change in curve profile at 40 mm indicates the interface of the two rings. The fact that the radial stress at the interface is negative indicates that there is no loss in contact between the two components at the interface. The radial stress at the interface will be referred to as the contact pressure (CP) throughout the document.

Figure 3-6 shows the radial stress calculated at the shaft OD at different rotating speeds. The results can be used to see at which rotating speed the hub will lose contact with the shaft. Figure 3-6 indicates a negative 65 MPa radial stress at zero speed due to the interference of the components. However, as the rotating speed increases the interference is relieved and the radial stress at the shaft OD becomes more positive. When eventually the radial stress becomes positive, it is interpreted as a loss in contact between the components at the interface. The loss in contact can result in rotor instability due to a large unbalance force and lead to catastrophic failure. The results from Figure 3-6 show that the hub will lose contact with the shaft at just under 29 000 r/min for this particular interference, geometry and material properties.

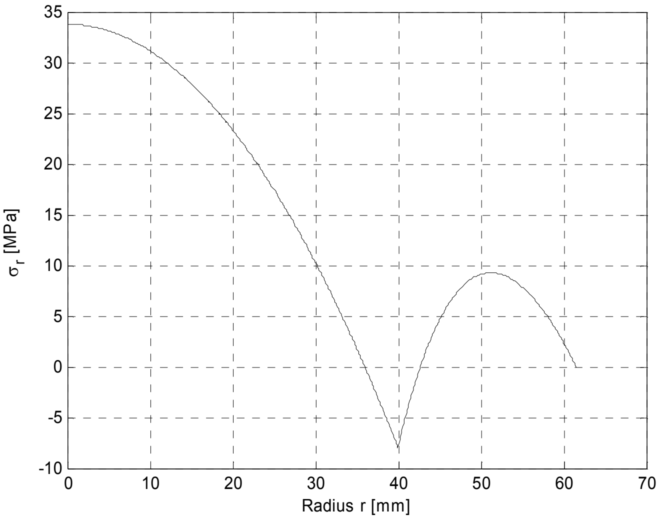

Figure 3-5: Radial stress in a rotating two ring shrink fitted assembly

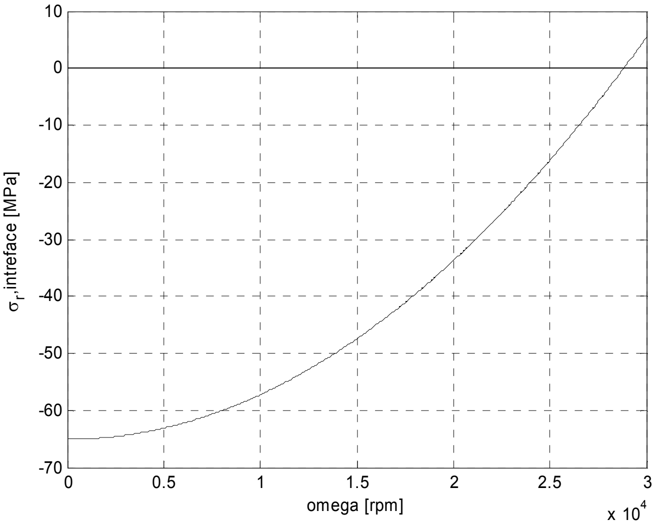

Figure 3-6: Radial stress at the interface at different rotating speeds

Figure 3-7 shows the tangential stress in both the components, similar to the radial stress plot described earlier. The major jump in stress at a radius of 40 mm indicates that a large tension is present at the ID of the hub, due to the interference. The tangential stress is also the main contributor to the maximum stress shown in Figure 3-8 which is the Von Mises equivalent stress. The results clearly show the problem with high material stress due to an interference fit, as mentioned in the literature.

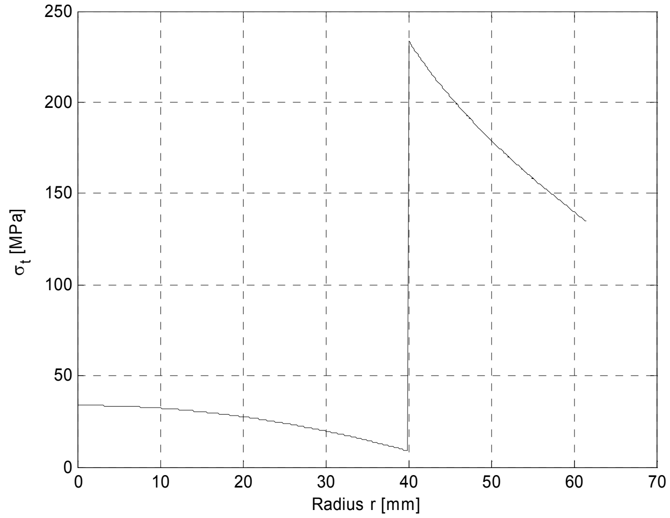

Figure 3-7: Tangential stress in a rotating two ring shrink fitted assembly

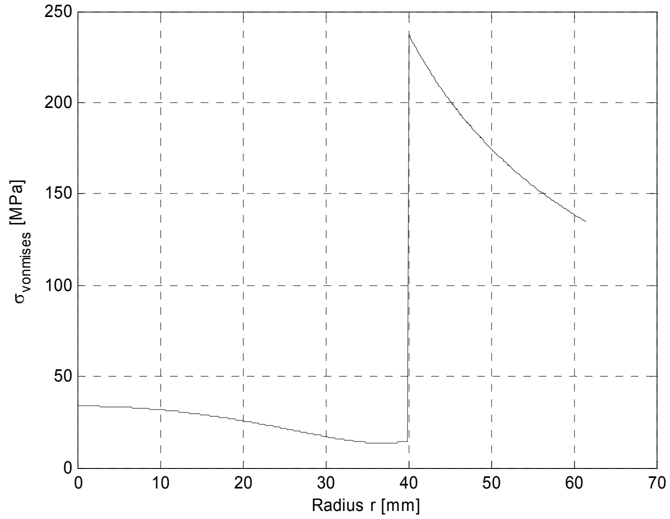

Figure 3-8: Equivalent Von Mises stress in a rotating two ring shrink fitted assembly

With this design tool, preliminary calculations on the required interference can be made. Table 3-3 shows the minimum interference required for each shrink fitted component, operating at 27,000 r/min. The table also shows the maximum Von Mises stress found in the component and the minimum required material yield strength for each component. Table 3-3 illustrates that for the rotor to be operated at 27,000 r/min the lamination material require a minimum yield strength of 444 MPa, which is achievable with high strength silicon steel lamination material. The results also show that if a copper alloy is used for the end rings, a yield strength of 504 MPa is required. Glidcop® Al-60 is a copper alloy that will satisfy the strength requirements. However, if an aluminium alloy is used for the end rings, most aluminium alloys will satisfy the strength requirements.

Table 3-3: Preliminary material selection and interference calculations

Component	Material	Required interference (µm)	Radial position of maximum stress (mm)	Maximum stress (MPa)	Required material strength (MPa)
Lamination	Silicon steel	90	40	222	444
End ring	Al alloy	150	40	93	186
End ring	Cu alloy	170	40	252	504

The results shown in Table 3-3 support the earlier calculations and suggest that the design speed can readily be achieved with available materials. However, Larsonneur's calculations are based on a solid outer ring which is not the case in the core of an IM. The squirrel cage is imbedded into the core and bar slots are required to accommodate the conductive bars. From the literature it is shown that these bar slots will result in a large stress concentration. Consequently, the stresses shown in Table 3-3 will not be the maximum stress in the IM outer ring. The literature indicates that the maximum stress would occur at the root and tip[7] of the slot, which seems logical, due the dominant stress in the outer ring being tangential. The outer ring could also be seen as a straight piece of material in tension with holes in it, which results in stress concentrations.

3.4.2 Analytical stress concentration factor

In order to analytically calculate the maximum stress in the outer ring with bar slots, stress concentration factors (K_t) were investigated. Figure 3-9 illustrates, Paterson's [48] stress concentration factor graph, for a single rotating disc with a hole at a radius. The K_t factor can be used to calculate the stress at the root and tip of the hole. There are a few parameters that influence the magnitude of the K_t value namely: The ratio of the hole position and outer radius of the disc (R_0/R_2), as well as the ratio of hole radius and outer radius of the disc (R_1/R_2). With these ratios known the K_t factor can be read off the graph. In order to implement the factor the tangential stress at the hole position is calculated for a disc with no holes and is multiplied with the factor to produce the stress at that position. Using the MATLAB® simulation the tangential stress can be calculated and the maximum stress is found.

With the selection of preliminary bar slot positions, the required ratios can be calculated and the stress concentration factor can be found for a specific design. Assuming R_0 = 55 mm, R_1 = 5 mm and R_2 = 61.5 mm the stress concentration factor $K_t \approx 2.8$ can be found. However, the ratio (R_0/R_2) falls outside the graph making it difficult to find the exact K_t value. Furthermore the exponential increase of the K_t value as the (R_0/R_2) ratio increases beyond 0.5 can result in a large error in the K_t value. However, using this value and calculating the stress at the root of the bar slot (r = 50 mm, δ = 90 µm and ω = 27,000 r/min) for the laminations, indicate a tangential stress of 170 MPa. Multiplying this with the K_t value results in a maximum stress of 476 MPa, with a FOS = 2 the required material's yield strength is 952 MPa. The newly calculated maximum stress is considerably higher than the 444 MPa as shown in Table 3-3. The maximum stress in the end rings can be calculated in a similar manner and also shows a considerable increase. The results indicate that traditionally used silicon steel lamination material cannot be used for

---

[7] The root and tip of the conductive bar slot represents the bottom and top of the slot respectively, as illustrated in Figure 3-3.

this high speed application. Nor will aluminium or copper alloys adhere to the stringent material strength requirements of the end rings in this high speed application.

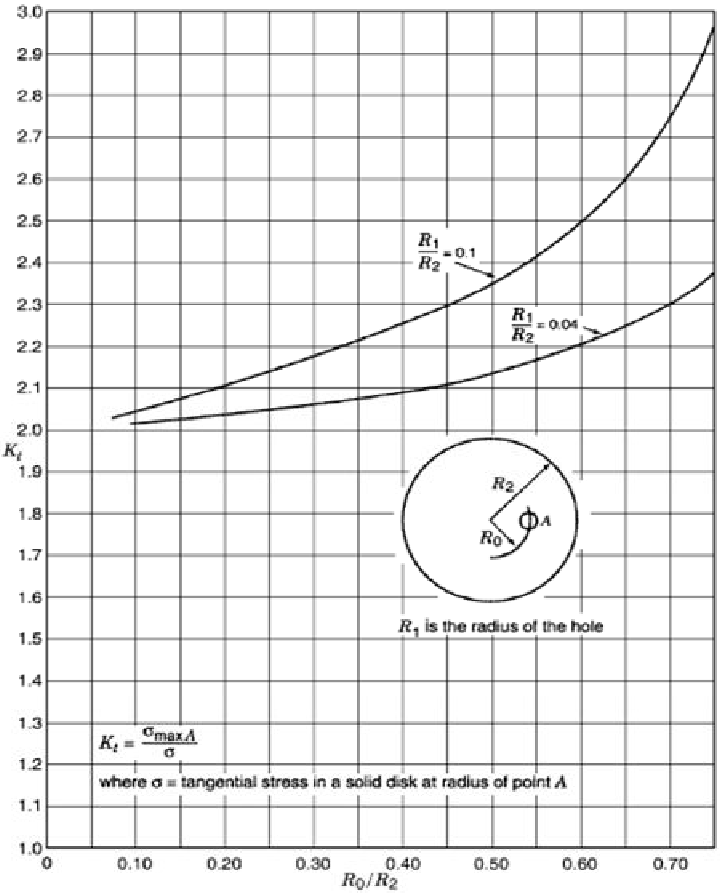

Figure 3-9: Paterson's stress concentration factor graph [48]

The accuracy of the maximum stress calculated with the stress concentration factor is however, in question, due to the extrapolation required to find the K_t value. Furthermore the stress in a rotating disc is similar to that of a rotating shrink fitted disc assembly, with the dominant stress component being the tangential stress. However, the radial stress due to the interference fit is ignored in the Paterson's stress concentrations shown in Figure 3-9. Consequently, the analytical calculations should be verified, this is done and described in the following section.

3.5 Verification of the analytical stress concentration

Using SolidWorks® Simulation, the stress concentration factor can be verified. The following section describes the verification systematically. The first step in verifying the stress concentration factor would be to verify the analytic calculations of a solid ring shrink fitted onto a solid shaft. The addition of bar slots in the outer ring can then easily be added to the simulation model. Also investigated is the implementation of finite element analysis (FEA) fixtures, constraints and affects of mesh size, to ensure the simulation represents reality.

3.5.1 Verification of stress in a solid outer ring

The analytical calculations are based on a thin solid ring (planar strain) with no bar slots, shrink fitted onto a solid shaft as shown in Figure 3-10. The components used in the simulation are modelled with the appropriate interference at the shaft/outer ring interface and a shrink fit is specified in the simulation. The model is constrained in the axial direction. The constraint is applied to the face on the one side of the assembly preventing the model to move in the axial direction. However, allowing the model to displace freely in the radial direction under load. After applying the constraints, the rotation and temperature loads can be applied to the model. Comparing the finite element model (FEM) and analytical results shown in Figure 3-11 and Figure 3-12 one can see an excellent correlation.

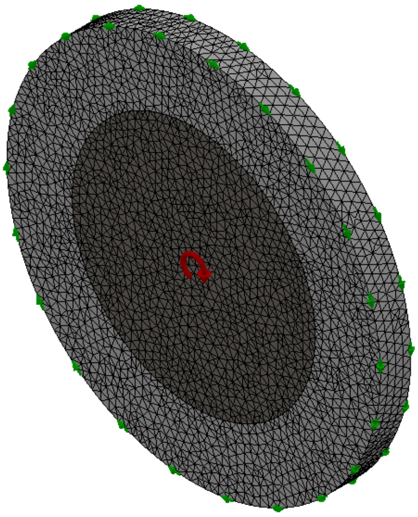

Figure 3-10: Full FEM model for a solid shaft and shrink fitted solid outer ring

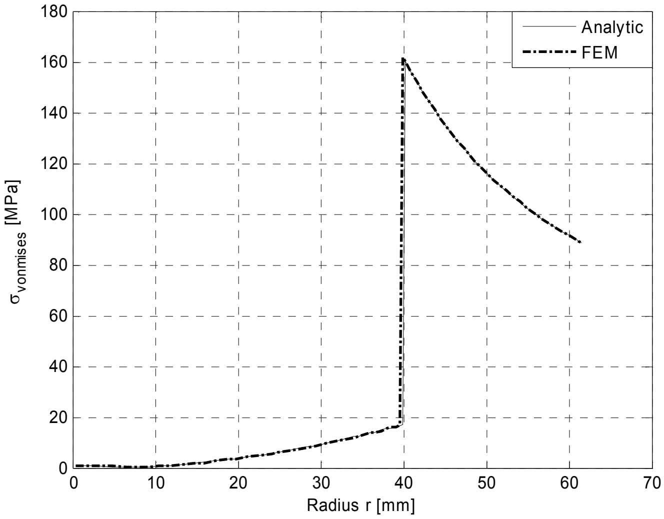

Figure 3-11: Comparison of analytical and FEM calculated Von Mises stress

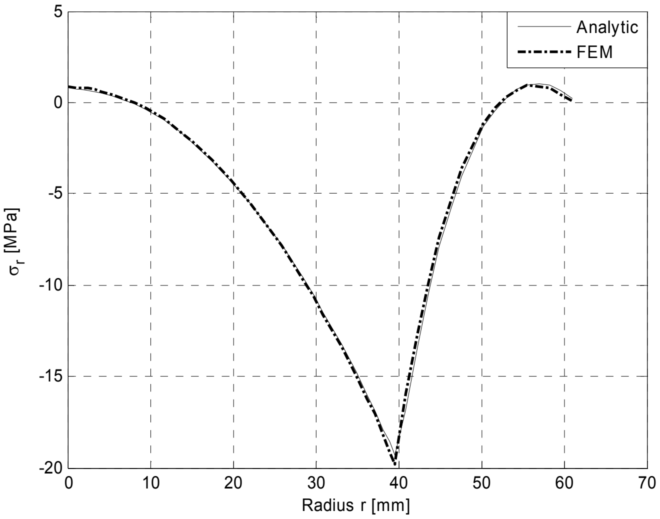

Figure 3-12: Comparison of analytical and FEM calculated radial stress

The FEM results verify the analytical calculations for a shrink fitted solid outer ring and confirms that any one of the two methods can be used. The next step would be to verify the use of the symmetry function, allowing the designer to model only a section of the complete model.

3.5.2 Verification of the FEM symmetry function

The use of the symmetry function is purely to save computation time. From Figure 3-10 and Figure 3-13 it can be seen that the element size is exactly the same in both models however the 1/24 section model will solve much faster. This is due to the fact that it only has 1/24th of the number of elements of the full model. This reduction in the number of elements will be of great significance in the more complex full motor assembly model described later in the chapter.

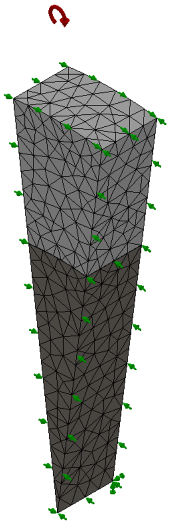

Figure 3-13: 1/24 section FEM of a solid shaft and shrink fitted solid outer ring

After simulating the full and 1/24 section models with exactly the same material properties and operating conditions, the results can be compared. Figure 3-14 and Figure 3-15 shows the radial and Von Mises stress as calculated in the full and 1/24 section models.

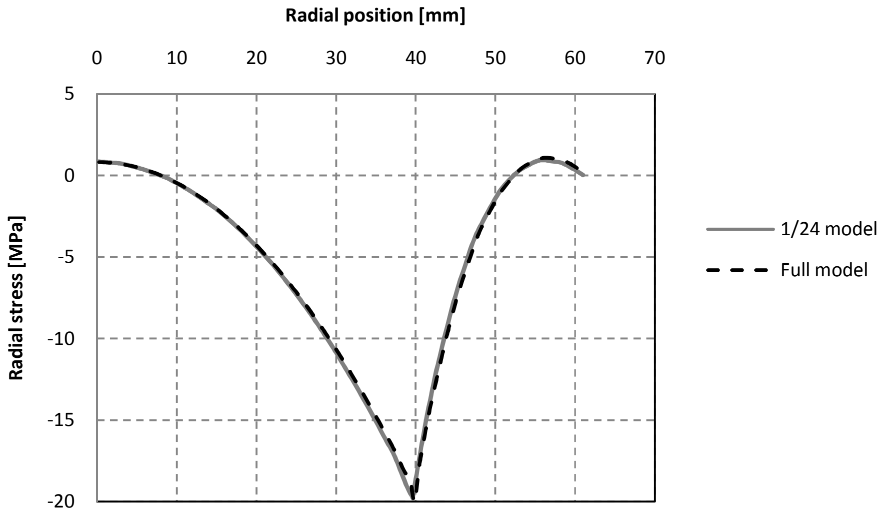

Figure 3-14: Comparison of the FEM calculated radial stress of the full and 1/24 section models

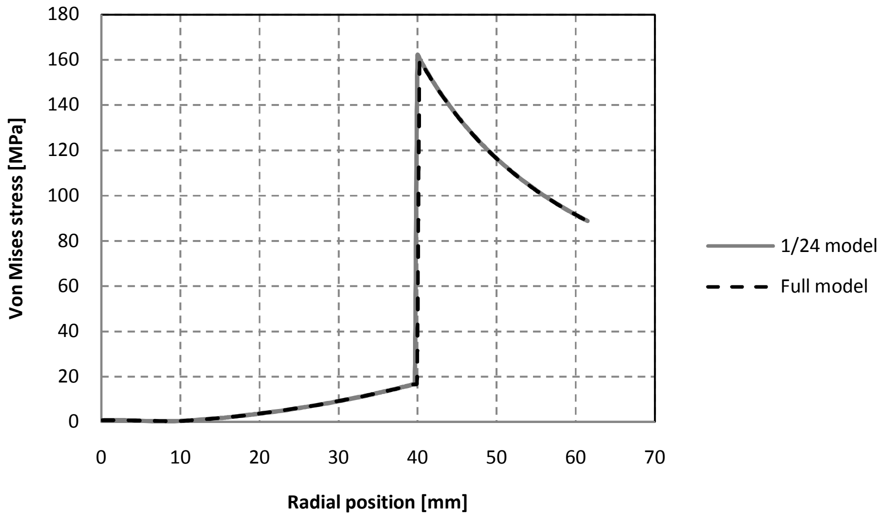

Figure 3-15: Comparison of the FEM calculated Von Mises stress of the full and 1/24 section models

These results verify the use of the symmetry function and indicate that the 1/24 model can be used in future analysis. The results also indicate that the model is simulated correctly and the bar slots can be added to the model in order to verify the stress concentration factor.

3.5.3 Verification of analytical stress concentration factor

Using the verified 1/24 section FEM and including the conductive bar slots as shown in Figure 3-16, the stress concentration factor can be calculated. Since stress concentrations are normally on a very small section of the component, the mesh size could influence the results. The optimum mesh size was obtained using an iterative process. The first step was to run both a simulation with the smallest mesh size possible as well as a relatively large mesh size for the same model. The results showed that the relatively large mesh simulation has a lower maximum stress, indicating that the mesh size should be decreased. A third simulation was then run with an intermediate mesh size and the results were compared to the smallest mesh size simulation. If the results indicated a reduction in mesh size was required then the intermediate mesh size simulation would become the new large mesh size simulation and a new intermediate mesh size was selected. This process was repeated until the stress of the intermediate and fine mesh simulations converged. The process ensures that a small enough mesh is used, to ensure correct results, without compromising on the computation time the simulation requires.

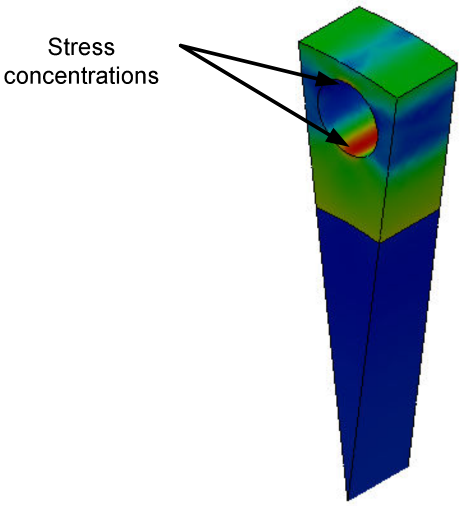

Figure 3-16: 1/24 section FEM of a solid shaft and shrink fitted outer ring with bar slots showing the stress concentrations positions

After systematically verifying the use of the section model with the bar slot included and establishing the required mesh size, the stress concentration factor can be verified. The results are extracted from the FEM analysis to compare it to the analytically calculated results. The Von Mises stress comparison is shown in Figure 3-17 and the dotted line represents the FEM results. With the bar slot's position at a radius of 55 mm and the slot in this case being circular, with a diameter of 10 mm, the stress concentrations will be at a radius of 50 mm and 60 mm respectively. From Figure 3-17 the FEM result shows a 403 MPa stress at r = 50 mm compared to the 206 MPa analytically calculated for a solid outer ring. Consequently the FEM results indicate a stress concentration of K_t = 1.96 compared to the K_t = 2.8 found from Paterson's graph. Furthermore, Figure 3-17 indicate a K_t = 2.41 at a radius of 60 mm, where the Paterson's graph show a K_t value in access of 3.5. Due to the considerable difference in the K_t values, the stress concentration is investigated further.

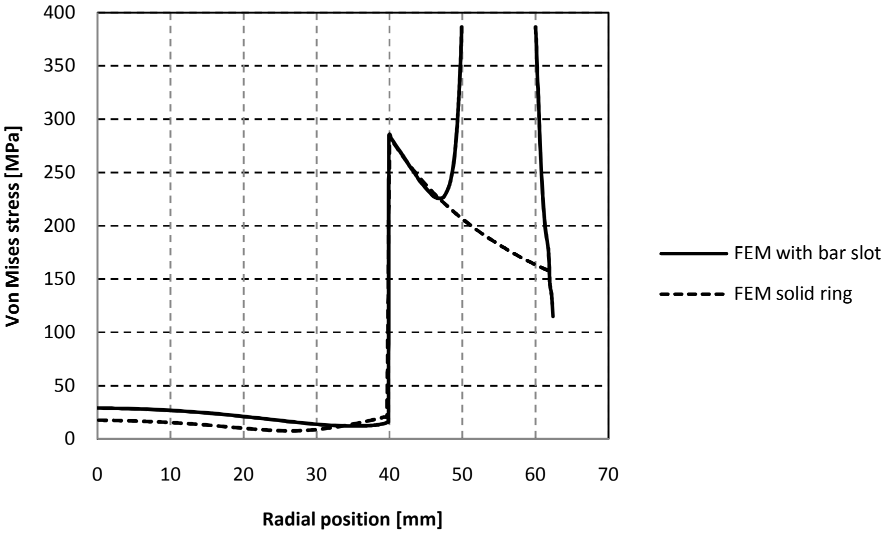

Figure 3-17: Verification of analytic stress concentration factor

3.6 Validating the stress concentration factors

As seen from the FEM and analytical calculations that include the stress concentration factor, the maximum stress is no longer at the ID of the outer ring. The results clearly indicate that the maximum stress is now found at the root and tip of the bar slot. Furthermore, the two methods used to calculate the maximum stress, indicate a considerable difference. Consequently, it was decided to validate the stress concentration by measuring the stress at the root and tip of the slot, using strain gages and scaled-up models (test rotors).

The following sections will describe work done on a similar project and how the knowledge gained was implemented during the validation of the stress concentration factor.

3.6.1 Dynamic stress measurements on a multi-ring test rotor

The ideal would be to measure the dynamic stress, at the stress concentration position, during rotation of the test rotor. It is however, exceptionally difficult to accurately measure the stress in a rotating disc. Extensive dynamic measurements were taken on a dynamic test rotor which proves this statement [43].

The work done on dynamic stress measurements was done on a multi-ring rotor, comprising the shaft and three solid shrink fitted rings, each consecutive ring made of a different material. Initially nine strain gages were installed onto the face of the rotor as indicated in Figure 3-18. Three strain gages were installed to measure the radial strain at or as close to the interfaces of the rings as possible. Only three radial measurements are required because the radial stress at the OD of the inner ring is equal to the radial stress at the ID of the outer ring [3]. The radial stress is monitored at these positions to validate the contact pressure between the shrink fitted rings during rotation.

Six tangential strain gages were also installed as close to the interfaces as possible and are situated on the ID and OD of each ring. This is due to the fact that the tangential stresses at the OD of the inner ring and ID of the outer ring are not equal. In order to plot a stress distribution graph as shown in Figure 3-17 both the radial and tangential stresses at the ID and OD are required.

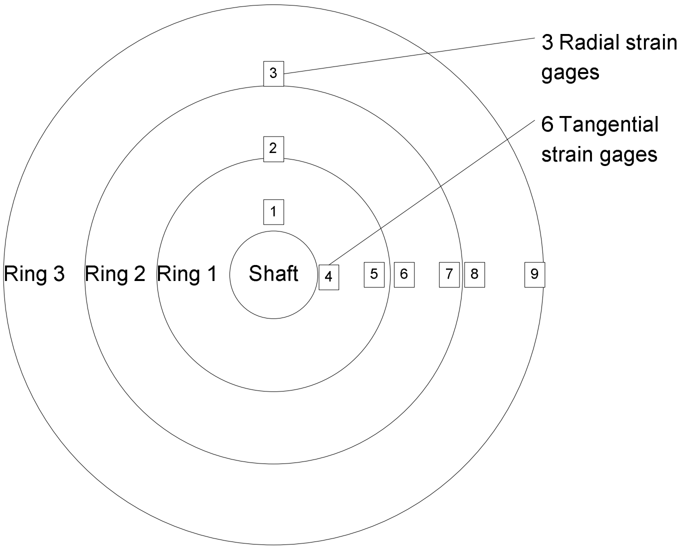

Figure 3-18: Strain gage positions on multi-ring dynamic test rotor [43]

The strain gages could only be installed after the rings were shrink fitted, therefore the dynamic measurement will only be that of the stress due to centrifugal forces, excluding the stress due to the shrink fits. One of the biggest problems was to monitor the signal of the strain gages during rotation. Two options were available namely, telemetric measuring equipment or the use of slip rings, each with its own set of problems. However, budgetary constraints ruled out the procurement of telemetry measuring equipment. Consequently, slip rings were installed onto the shaft as indicated in Figure 3-19. The slip rings are made of a copper alloy and the brushes are made of carbon.

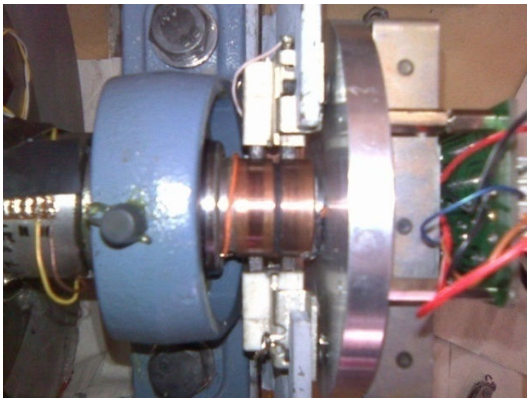

Figure 3-19: Slip ring integration onto dynamic test rotor [43]

Strain gage signals are very small and always require amplification in order to have a measurable signal [49]. The fact that only the stress due to the centrifugal force is measured further suggests that the signals will be relatively small. First order calculations support the notion and it was established that the signal must be amplified considerably, before going through the slip rings. This is done to eliminate any amplification of an error due to the change in resistance of the carbon slip rings. Therefore an amplifier was installed onto the shaft as shown in Figure 3-20. However, even with a 47,000 times amplification, initial calculations showed that a relatively small (voltage < 1 V) signal will be produced.

The strain measured was limited due to the limiting rotational speed, which was limited to 2700 r/min. The main reasons were safety considerations and questions regarding the mechanical and electrical integrity of the amplifier under centrifugal forces and variations in slip ring resistance.

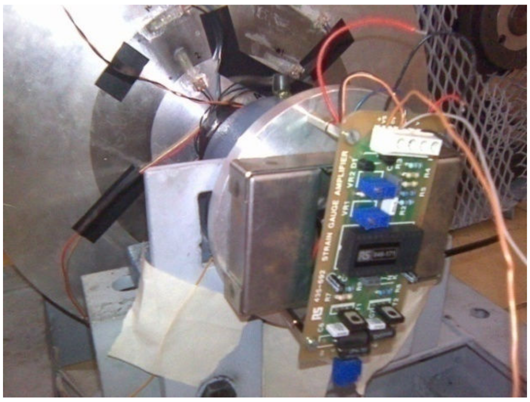

Figure 3-20: Illustration of strain gage amplifier integration [43]

In order to establish the affect of the centrifugal forces on the amplifier and the affect of continuous operation of the slip rings, extensive testing was done to characterise the system. The tests were interpreted and compensation factors were included in the measurements. The dynamic test results shown in Figure 3-21, illustrate both the calculated and measured radial stresses. Figure 3-21 indicates that the measured results have a similar stress profile compared to the calculated results. However, the measured stress is between 60% and 35% less than the calculated stress.

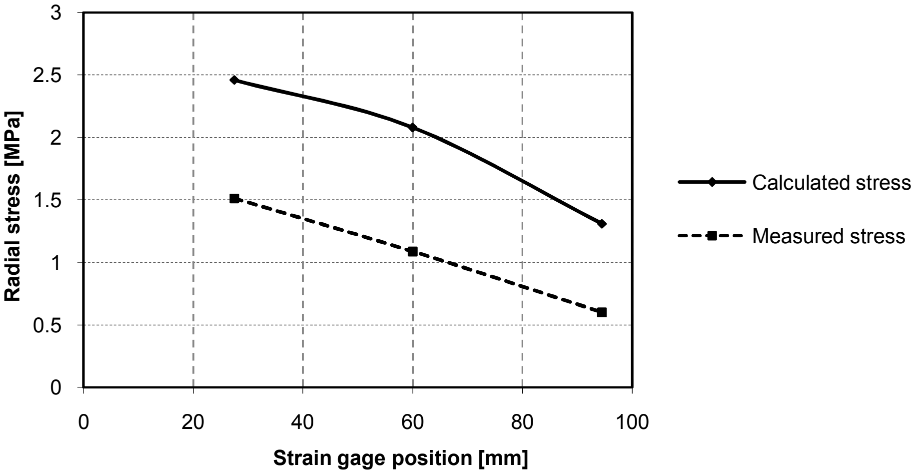

Figure 3-21: Dynamic test rotor radial stress measurements [43]

Figure 3-22 compares the dynamic measured and calculated tangential stress and similar to the radial measurements, the stress profile shows a good correlation. However, the measured stress is between 45% and 30% less than the calculated stress.

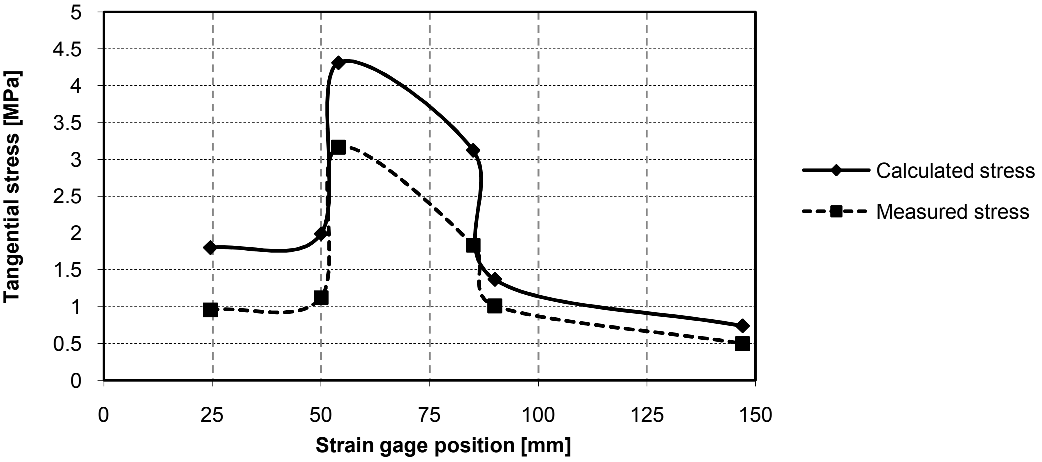

Figure 3-22: Dynamic test rotor tangential stress measurements [43]

After realising that both the radial and tangential measurements have a similar stress profile but seems to be a fraction of the calculated stress, the gage positions and installation were investigated. Two additional gages were installed on the outer surface of the dynamic test rotor with the one gage as indicated in Figure 3-23 and the other directly opposite.

Figure 3-23: Illustration of the additional tangential strain gage position at the outer surface of the dynamic test rotor

The measured results of the additional strain gages are shown in Table 3-4 and the results indicate that the two measurements are within 10% of each other and within 5% of the calculated stress. The difference in measurement can be credited to a number of reasons. For one the orientation of the gages cannot be 100% the same and the measuring equipment and slip rings will have an influence.

Table 3-4: Dynamic stress measurements of the additional tangential strain gages

	Calculated	Gage 11	Gage 12
Stress (MPa)	0.72	0.681	0.755
Error (%)		-5.35	4.83

Due to the results of the two additional gages, one can assume that the measurements of the gages installed on the face of the rotor are incorrect. However, the measurements indicate the same stress trend through the multi-ring rotor, but seem to only measure a fraction of the total stress. This is attributed to the fact that the gages measure the average strain over a relative small surface (6 x 2 mm) and not on a specific point, as is the case in the analytical calculations. This statement is further investigated and the effects illustrated in section 3.6.2. Furthermore, the tangential stress at the OD of the rotor is constant over the entire surface and due to this, the strain gage measurements will be close to that value. The additional two strain gage results, gives confidence in the analytic calculations and confirms that the gages installed on the face of the rotor only measure the average stress over the area.

In conclusion the results indicate that it is not possible to accurately measure the radial or tangential stress at a specific point on the face of the dynamic test rotor. The test also indicates that a relatively small strain gage signal is produced due to the rotational speed limit. It will be shown in section 3.6.2 that the knowledge gained through these tests can be implemented in order to validate the stress concentration factor using strain gage measurements.

3.6.2 Stress measurements on a static test rotor with bar slots

Extensive calculations and measurements were done on the dynamic test rotor, however, it is not an accurate representation of an induction machine rotor. Furthermore, the results found from the dynamic stress measurements indicated that accurate dynamic measurements are difficult to obtain. Consequently a new test rotor was constructed with the main focus on the maximum tangential stress at the root and tip of the bar slot. Initial calculations showed that if the current dynamic test setup is to be used the stress difference between 0 r/min and 2700 r/min will only be 0.9 MPa. This difference is less than the expected error in measurement and therefore it was decided that a stationary rotor setup will be sufficient. The stationary test rotor will be used to validate the FEM simulation’s stress concentration at the root and tip of the bar slots.

The test rotor is a 2.4 times scaled-up model of the induction machine rotor[8]. The scaling is done purely to allow for installation of the strain gages, at the positions as indicated in Figure 3-24. The final dimensions for the test rotor is; shaft OD ≈ 192 mm, outer ring OD ≈ 295 mm and bar slot diameter 24 mm at a radius of 132 mm. The thickness of the components is 35 mm which is adequate to ensure that no buckling will occur. After the manufacturing of the components an actual interference of δ_d = 202µm was measured using a high precision 3D measuring machine at Denel Dynamics Pty Ltd. The material selected for the shaft is EN8 and the outer ring is made of aluminium 6082-T6. The reason for the

---

[8] The stationary test rotor is scaled with reference to the rotor dimensions as indicated in Table 3-2

aluminium outer ring is to allow disassembly of the test rotor, allowing for multiple tests. For the outer ring to be removed the rotor assembly is heated up to 220 °C at which point the outer ring's ID will be 160 µm larger than that of the shaft's OD and the shaft can be removed. This is due to the large difference in thermal expansion coefficients between the shaft and outer ring material.

The test rotor was also designed to evaluate two bar slot configurations which is illustrated in Figure 3-24. The rotor included both slitted and non-slitted bar slots as indicated with the "stress relieving and no-stress relieving cut" annotations. Figure 3-24 also indicates the strain gage positions, where gages 1 and 2 are installed at the root of two slitted slots. Gages 3 and 5 are installed at the roots and 4 and 6 at the tips of two opposing bar slots with no stress relieving cuts.

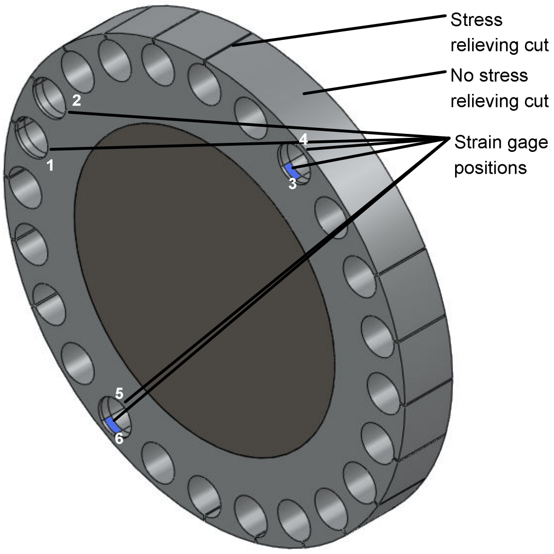

Figure 3-24: Illustration of the FEM model used to calculate the stress at the strain gage locations

Figure 3-25 (a) illustrates the shrink fitted static test rotor with the six strain gages installed, (b) illustrates a detail view of a single gage. The detail view indicate the position and relative size of the strain gage, the gages were installed as close as possible to the stress concentration position.

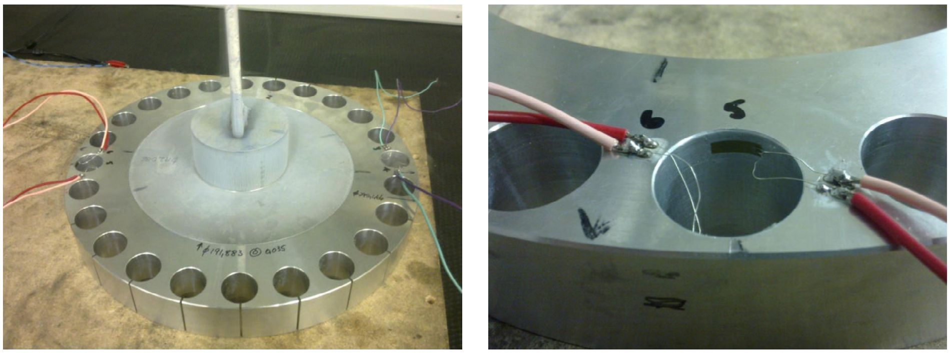
(a) (b)

Figure 3-25: (a) illustrates the static test rotor after shrink fit and (b) is a detail view of two of the strain gages

Figure 3-26 illustrates the FEM tangential stress result of the static test rotor. This model is used to calculate the stress at the strain gage positions and the results are tabulated in Table 3-5, Table 3-6 and Table 3-7. The tables show the maximum, minimum and root mean square (RMS) stress values of the area where the gages are installed as well as the measured tangential stress at these positions. The tables also include a description on the relative position of the gages for a better interpretation of the results.

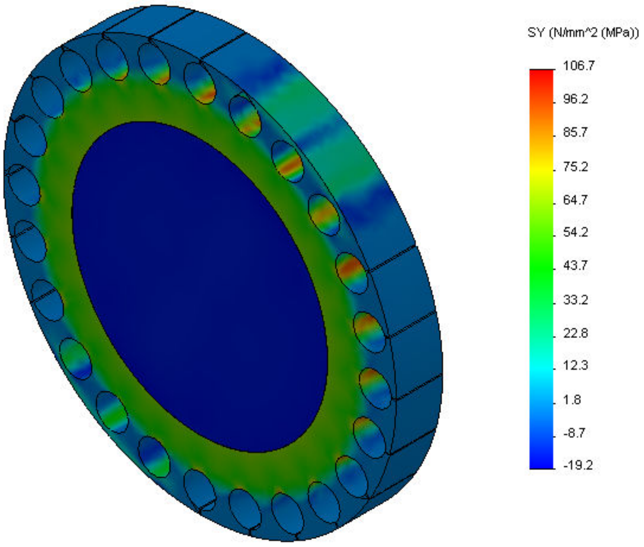

Figure 3-26: Static test rotor FEM tangential stress results

The measuring equipment used for the strain gage measurements is calibrated using a simple cantilever beam test setup as illustrated in Figure 3-27. This simple setup allows accurate stress calculation at the strain gage positions which is used to characterise the strain gage amplifier.

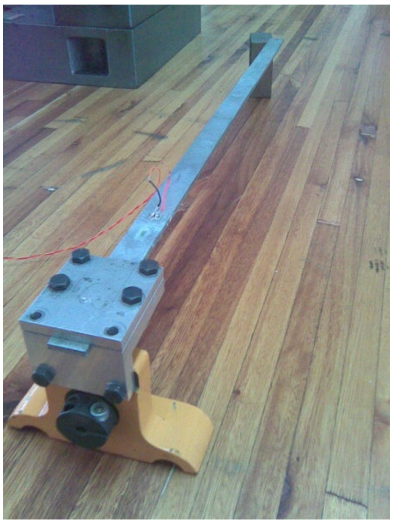

Figure 3-27: Cantilever beam test setup used for calibration

Table 3-5 shows the measured and calculated results of the two gages installed at the root of two bar slots, both with a stress relieving cut. The FEM results are calculated for the ideal strain gage position and were not changed according to the actual position. The relative position-descriptions indicate that the gages are very close to the same position and orientation. However, the gages are not perfectly at the stress concentration position as indicated by the 1 mm offsets.

Table 3-5: Tangential stress calculated and measured at strain gage 1 and 2

Strain gages at root of bar slot with stress relieving cut						
Gage 1: Relative position			**Gage 2: Relative position**			
3 mm from top face 1 mm to the right of stress concentration Not 100% parallel to face			3 mm from top face 1 mm to the right of stress concentration Not 100% parallel to face			
Measured	Voltage (V)	2.045	**Measured**	Voltage (V)	2.09	**Difference (%)**
	Stress (MPa)	**84.78**		Stress (MPa)	**86.65**	**2.20**
FEM	Max (MPa)	97.058	**FEM**	Max (MPa)	97.154	
	Min (MPa)	72.946		Min (MPa)	72.889	
	RMS (MPa)	88.564		RMS (MPa)	88.605	

The measured results of strain gage 1 and 2 has a difference of only 2.2 % and although it is close to impossible to get this 100 % the same, the results indicate that the measurement is correct. The small difference in measurement also supports the description of the relative position.

Gage 1 and 2 indicates measurements of only 87.3 % and 89.2 % respectively, of the maximum FEM calculated stress. However, the results also indicate that the measured values are very close to the RMS calculated stress. Gage 1s measurement indicates a stress of 4.3 % below its calculated RMS value and gage 2s measurement is 2.2 % lower than its calculated RMS value.

Table 3-6 shows the measured and calculated results of the two gages installed at the root of two bar slots, both with no stress relieving cut. The relative position descriptions of the gages indicate that a variance in measurement is to be expected. The results indicate a difference of 10.23 % between the two strain gage measurements which can largely be credited to the difference in positions and orientation.

The results indicate that gage 3 measures only 82.1 % and gage 5 measures 90.6 % of the calculated maximum stress. Gage 3 and 5 are also 9.5 % and 0.5 % less, respectively than the RMS calculated stress value. Both these percentages further support the relative position description, where it is indicated that gage 5 is much closer to the ideal position then gage 3.

Table 3-6: Tangential stress measurement at root of bar slots with no stress relieving cut

Strain gages at root of bar slot with no stress relieving cut						
Gage 3: Relative position			**Gage 5: Relative position**			
2 mm from top face 2 mm to the right of stress concentration Not 100% parallel to face			2 mm from top face 0.5 mm to the left of stress concentration Almost 100% parallel to face			
Measured	Voltage (V)	1.769	**Measured**	Voltage (V)	1.95	**Difference (%)**
	Stress (MPa)	**73.34**		Stress (MPa)	**80.85**	**10.23**
FEM	Max (MPa)	89.339	**FEM**	Max (MPa)	89.26	
	Min (MPa)	65.899		Min (MPa)	66.209	
	RMS (MPa)	81.024		RMS (MPa)	81.224	

Table 3-7 shows the measured and calculated results of the two gages installed at the tip of two bar slots, both with no stress relieving cut. The results indicate a difference of 12.57 % in the measured stress and this can largely be credited to the difference in gage positions. Similar to the previous 4 strain gage results the measurement is lower than the maximum calculated stress. Gage 4s measurement is 78.9 % and gage 6, 89.8 % of the maximum calculated stress. The results also indicate that gage 4s measurement is 10.1 % less and gage 6s measurement is 2.6 % more than the calculated RMS stress value.

The fact that gage 6 measurement is closer to the maximum calculated stress compared to gage 4, is due to the fact that gage 6 is closer to the ideal stress concentration position. The variation due to position is described in more detail in the following section.

Table 3-7: Tangential stress measurement at tip of bar slots with no stress relieving cut

Strain gages at tip of bar slot with no stress relieving cut						
Gage 4: Relative position			**Gage 6: Relative position**			
2mm from top face 2mm to the left of stress concentration Almost 100% parallel to face			2mm from top face 0.5mm to the right of stress concentration Almost 100% parallel to face			
Measured	Voltage (V)	0.835	**Measured**	Voltage (V)	0.94	**Difference (%)**
	Stress (MPa)	**34.62**		Stress (MPa)	**38.97**	**12.57**
FEM	Max (MPa)	43.896	**FEM**	Max (MPa)	43.414	
	Min (MPa)	28.21		Min (MPa)	28.02	
	RMS (MPa)	38.506		RMS (MPa)	37.99	

3.6.3 Conclusion of static stress measured results

From the results presented in Table 3-5, Table 3-6 and Table 3-7 it is apparent that the measured stress is only a portion of the maximum calculated stress. Table 3-8 summarizes these results and shows each gage's measurement as a percentage of the maximum calculated stress. The results clearly show that the percentage is closely linked to the gage relative position indicated by the "offset from optimum position". As the offset increases the measurement decreases.

The RMS value represents the average calculated stress over the strain gage area (6 x 2 mm). The area is modelled at the optimum gage position and the measured value is compared to the RMS value as a "percentage from the RMS" value in Table 3-8. In theory if the gages were exactly at the optimum position the measured and RMS stress values would be equal and a zero difference would be shown in Table 3-8. This is also proven by the measured results, which show the percentage difference decreasing as the offset decreases.

From these results the conclusion can be made that the strain gages measures the average strain over the entire gage area and the measurement can be compared to the FEM calculated RMS stress.

Table 3-8: Summary of strain gage measurements

	Gage number					
Parameter	**1**	**2**	**3**	**4**	**5**	**6**
Percentage from the RMS (%)	-4.3	-2.2	-9.5	-10.1	-0.5	2.6
Percentage of maximum stress (%)	87.3	89.2	82.1	78.9	90.6	89.8
Offset from optimum position (mm)	1	1	2	2	0.5	0.5

From these results it is apparent that the relative gage position is critical for consistent measurements. The difference in measurements of the gages installed at similar positions with only a small variation in position, can be explained using Figure 3-28.

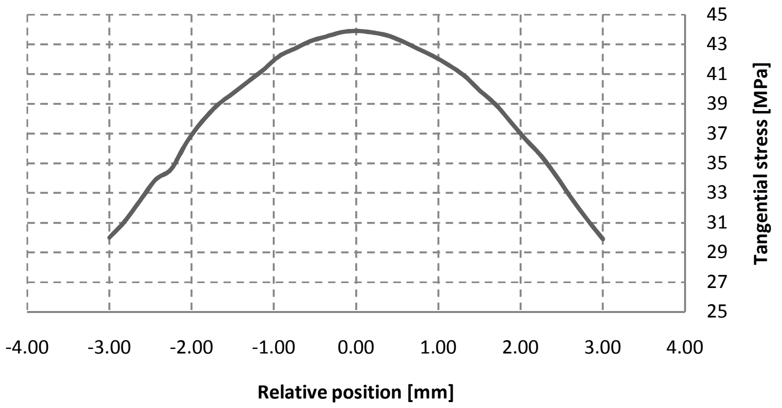

Figure 3-28: Tangential stress distribution at gage 4's position

Figure 3-28 illustrates the FEM calculated tangential stress over strain gage 4's ideal area and indicates that the stress distribution over the strain gage area changes considerably. The results indicate that the maximum stress is 43.896 MPa at the 0[9] position and 28.21 MPa at a ±3 mm offset. Consequently the results indicate that a small difference in placement can result in a large difference in measurement.

The results indicate that the measured tangential stress correlates closely to the FEM calculated RMS tangential stress value. From these results it can be assumed that if the stress could be measured at the stress concentration point it will be equal to the FEM calculated maximum tangential stress. Therefore, the measurements indicate that the Paterson's [48] stress concentration factor cannot be applied to this particular configuration and the FEM will be used throughout the detail design.

Due to the difficulty of measuring the stress in the final designed rotor at its maximum operating conditions a system was set in place to verify and validate the design tools used throughout the detail design. Therefore, the stress measured in the test rotors will not validate the stress in the final rotor. But rather validate the FEM simulation design tool, used during the detail design of the final rotor. Other forms of verification and validation on a system level are described in detail throughout chapter 5.

3.7 Detail IM mechanical design

During the detail mechanical design section, alternative conductive bar slot geometries are presented and the effect the geometry has on the maximum stress and contact pressure (CP)[10] is investigated. The section also includes final material selection and detail stress analysis of both the individual sub-assemblies as well as the complete IM rotor section. The rotor section FEM is used to calculate the final required interference and the allowable manufacturing dimensional tolerance.

3.7.1 Investigating the optimum bar slot design

Using the verified and validated FEM design tool, the effect of the bar slot geometry is investigated; Figure 3-29 shows the fringe plot of the Von Mises stress and a vector plot of the contact pressure (CP) at the interface of a solid outer ring model. Figure 3-30, Figure 3-31, Figure 3-32, Figure 3-33 and Figure 3-34 illustrate the same two plots, but for an outer ring with circular, oval and square bar slots respectively and some with other stress relieving cuts. The results show the effect the bar slots have on both the maximum stress as well as the contact pressure at the interface. All the slots have the same sectional area and the slot centres are at the same radial position. The simulation parameters for each study are exactly the same in terms of; constraints, amount of interference, rotational speed and material properties. Figure 3-29 shows a solid outer ring and is presented as a reference to easily see the effect the different bar slots have on the maximum stress and interference pressure.

---

[9] Ideal position for the stress concentration measurement

[10] Contact pressure (CP) refers to the radial stress at the interface of the shrink fitted components

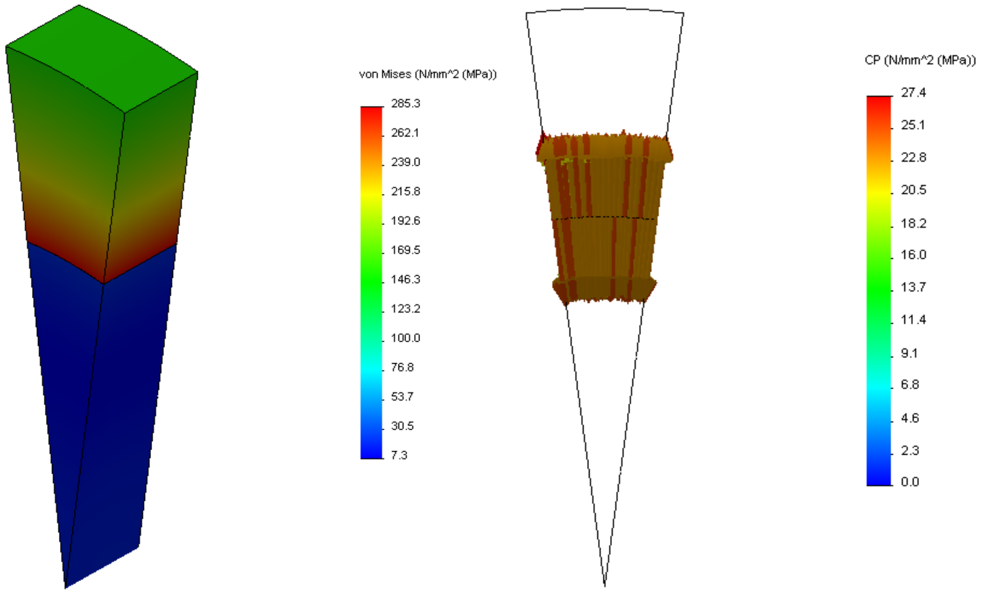

Figure 3-29: Von Mises stress and contact pressure at interface for a solid rotor

Figure 3-30 illustrates a circular slot with a maximum Von Mises stress of 403.3 MPa and a maximum CP of 17.7 MPa. However, the maximum CP is not a good indication of the true interference at high speed and a better measure is, the average value as summarised in Table 3-9.

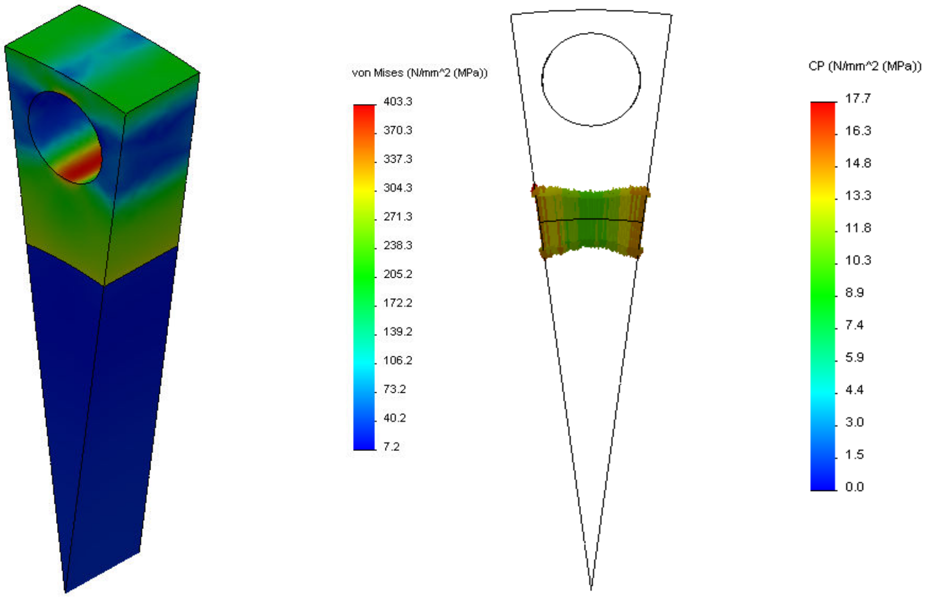

Figure 3-30: Von Mises stress and contact pressure at interface for a circular slot

Figure 3-31 is an illustration of a square slot which results in an increase in the maximum stress and decrease in the maximum CP as seen from the results. Figure 3-32 shows the affect of an oval slot and the results indicate that it has the lowest maximum stress of the three slot geometries. The maximum CP is also the highest of the three options. However, the manufacturing of both the square and oval slots would be very difficult and costly, it would need to be wire cut or spark-eroded. Consequently it was decided to use a circular bar slot which is the optimum solution considering manufacturing and cost.

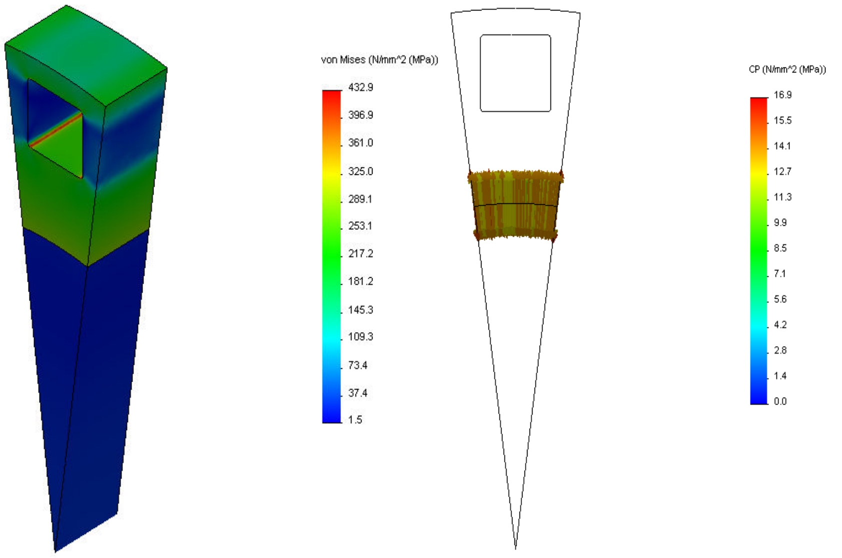

Figure 3-31: Von Mises stress and contact pressure at interface for a square slot

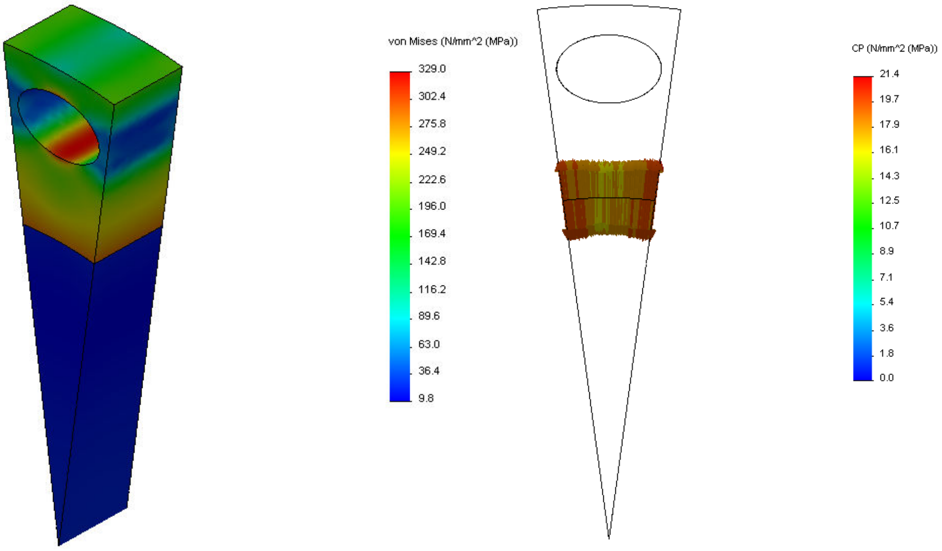

Figure 3-32: Von Mises stress and contact pressure at interface for an oval slot

After selecting the circular bar slot, some stress relieving cuts were investigated. From the literature [9] it is indicated that the bar slot can be interleafed with stress reliving slots as shown in Figure 2-7. However, the only effect is that the maximum stress is diverted to the stress relieving slots. The addition of the stress relieving slots can also increase the maximum stress as found in Figure 3-33 due to the geometry and position. This was useful in their design [9] because they had to divert the maximum stress away from the weaker welded joint. This type of stress relieving cut also reduces the CP significantly and would therefore require a larger interference fit, which in turn will increase the maximum stress.

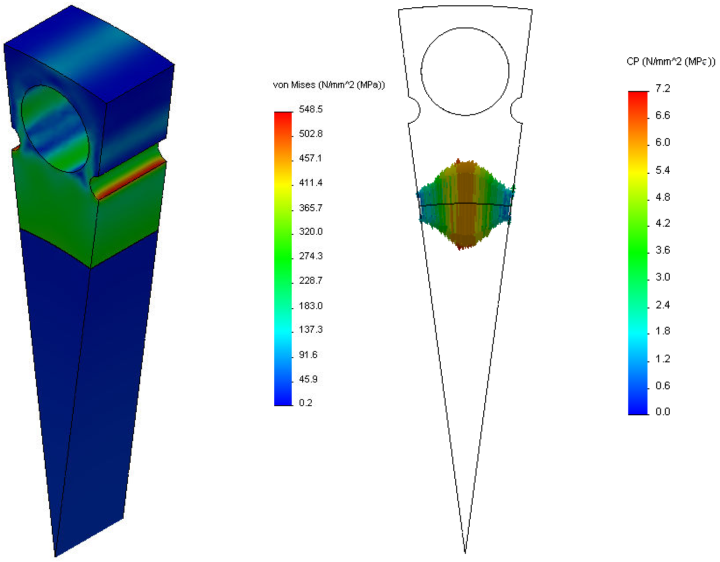

Figure 3-33: Von Mises stress and contact pressure at interface for a circular slot with stress relieving cuts

Another stress relieving cut which is also advantages to the electromagnetic design is a slitted rotor as indicated in Figure 3-34. However, the results indicate an increase in maximum stress and the CP is also dramatically reduced with the addition of this stress relieving slit.

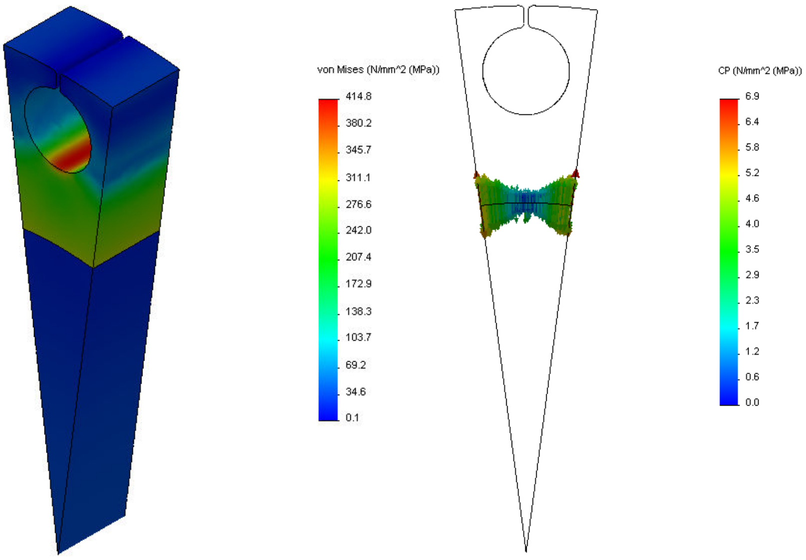

Figure 3-34: Von Mises stress and contact pressure at interface for a circular slot with stress relieving slit

Table 3-9 summarises the results shown above and indicates that the oval slot would be the best choice. Due to the oval slot having the lowest maximum stress and the smallest affect on the CP, however, due to manufacturing, this is not a viable option. Furthermore the results indicate that the stress relieving cuts reduce the CP dramatically. Therefore the best solution is to utilise a circular slot with no stress relieving cut.

Table 3-9: Summary of geometry affects on maximum stress and contact pressure

Reference Figure	Slot geometry	Stress reliving feature	Von Mises (MPa)	Contact pressure (MPa)		
				Average	Maximum	Minimum
Figure 3-29	No slot	None	285.3	24.16	27.16	21.59
Figure 3-30	**Circular**	**None**	**403.3**	**12.81**	**17.11**	**9.68**
Figure 3-32	**Oval**	**None**	**329**	**18.58**	**21.08**	**15.95**
Figure 3-31	Square	None	432.9	13.89	16.94	11.66
Figure 3-33	Circular	Keyhole	548.5	3.58	7.17	0.76
Figure 3-34	Circular	Slitted	414.8	2.81	6.16	0.13

3.7.2 Material selection and final dimension specifications

From the results found in the preliminary design calculations, it is seen that for a laminated aluminium cage rotor with a maximum operating speed of 27 000 r/min and OD 123 mm, the maximum stress σ_{max} is 450 MPa. Consequently the preliminary calculations with a FOS of 2 indicate that a minimum yield strength of 900 MPa is required for the lamination material. Furthermore, the literature shows that in order to obtain such high yield strength one has to compromise on the electromagnetic properties. The lamination material with the highest yield strength that could be obtained was Vacuumschmelze's Cobalt-Iron alloy (Vacodur S Plus) with a yield strength of 800 MPa. However, the material could not be delivered within the allowable budget or time period. This presented a problem and it was decided to use the lamination material with the highest yield strength that satisfies the electromagnetic requirements and is locally available.

Table 3-10 shows the material properties as it is used in the calculations (material certificate's included in the data CD). The shaft and spacers are made of AISI 4140. The lamination material selected is SURA® M270-35A produced by Cogent. M270-35A is the lamination material with the highest yield strength that has satisfactory electromagnetic properties, readily available by local suppliers. The copper alloys usually used for IM cages, as discussed in section 2.3, was not available at local steel suppliers. Due to the time constraints and the availability of aluminium alloys it was decided that the cage will be fabricated from the best suitable aluminium alloy. Material selected for the end ring is Al 7075-T6. This alloy is known for its strength and is produced in a bar form of different diameters. Al 2024-T3 was selected for the conductive bars due to the lower strength requirements and because it is produced in a 12 mm bar, resulting in minimum material removal required.

Table 3-10: Material data as used in calculations

Material	Modulus of Elasticity E (GPa)	Yield strength σ_y (MPa)	Poisson's Ratio υ	Density ρ (kg/m^3)	CTE α (10^{-6}/°C)
AISI 4140 T-condition	205	760	0.285	7850	12.3
EN 10106 (M270-35A)	185	450	0.3	7650	12.0
Aluminium 7075-T6	72	516	0.33	2810	23.6
Aluminium 2024-T3	73.1	360.7	0.33	2780	23.2

With the maximum allowable stress in the magnetic core limited to 225 MPa, the preliminary calculations are used to calculate the revised operating speed. Table 3-11 shows the revised specifications which shows the speed to be reduced to 19 000 r/min and the reduction in speed implies that the machine's power delivery is reduced to 75 KW. This is not ideal, however, it was decided that a follow-up project will be defined and using the lessons learnt during the development of the 19 000 r/min rotor, a 27 000 r/min rotor can be developed.

Table 3-11: Revised drive specifications

Specification	Quantified	Description
Maximum operating speed N_{max}	18,500 r/min	Maximum operating speed with an over speed of 19,000 r/min
Ambient operating temperature T	80 °C	All temperature affected calculations are done with the assumption that the components are at an ambient temperature
Machine power	75 kW	The mechanical power required is derived from the blower specifications
No mechanical contact	N/A	Due to the application no lubrication can be used, as it will contaminate the coolant
Impeller interface	N/A	With the exclusion of a gearbox the blower can be attached directly to the machine shaft
Mechanical FOS	2	The Von Mises equivalent stress should be ≤ half the material's yield strength

Table 3-12 is a summary of all the IM component's dimensions as illustrated in Figure 3-35, the detail drawings is shown in Appendix B, these dimensions were obtained through an iterative process described in this section. During the iterative stress analysis, the amount of interference was change and the maximum stress and minimum CP was monitored until the results were within the allowable limits. The maximum interference is limited by the maximum allowable stress in the components. The minimum interference is limited by the fact that a contact pressure (CP) is required at the interfaces, for the maximum operating conditions. The shaft was measured with high precision equipment before the dimensional tolerances of the other components were calculated. This is done to minimise tolerance build-up, which would be detrimental for this type of application. Table 3-12 show the dimensions of the last iterations, for both the minimum and maximum allowable interference. From these results the dimensional tolerance of each component is found. The results also indicate that the dimensions are critical and the high speed machine requires very tight dimensional tolerance.

Table 3-12: Component dimensions as used in calculations

Part	Material	Interference MIN			Interference MAX		
		ID (mm)	OD (mm)	Interference δ_d (µm)	ID (mm)	OD (mm)	Interference δ_d (µm)
Shaft	AISI 4140 T-condition	0	80.0		0	80.0	
Lamination	EN 10106 M270-35A	79.936	123	64	79.930	123	70
Spacer	AISI 4140 T-condition	79.936	123	64	79.930	123	70
End ring	Aluminium 7075-T6	79.850	123	150	79.844	123	156
Conductive bar slot	N/A	0	10.005		0	10.000	
Conductive bar parallel interference fit end	Aluminium 2024-T3	0	10.010	5	0	10.030	30
Conductive bar dowel pin end	Aluminium 2024-T3	0	10.020	15	0	10.030	30

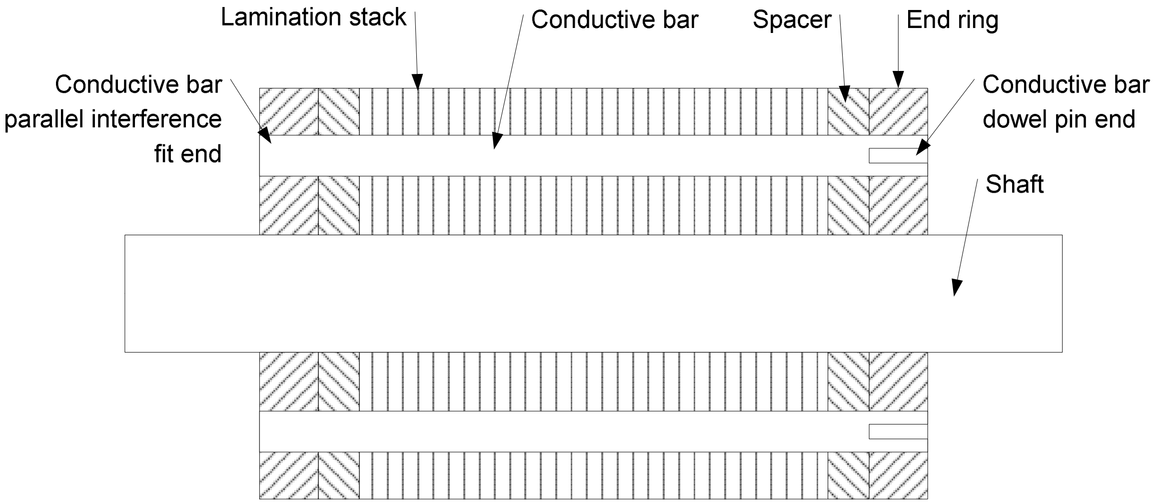

Figure 3-35: Illustration of IM rotor section layout

The maximum interference is obtained by limiting the maximum allowable stress. The minimum interference is the minimum amount of interference required for the hub to stay in contact with the shaft at maximum operating conditions. The difference between the minimum and maximum interference is the allowable manufacturing dimensional tolerance.

During the following sections the lamination, spacer and end ring sub-assemblies are considered individually after which the full assembly will be analyzed. The results will be compared in order to verify the full assembly. The results shown for the sub-assemblies will be the maximum stress due to the maximum interference and the CP for the minimum interference.

3.7.3 Detail magnetic core stress analysis

The following paragraph shows the stress calculated for the magnetic core (laminations) with the conductive bar included in the simulation as illustrated in Figure 3-36. The lamination stack for simulation purposes is seen as a solid material represented by a ring with a 10 mm thickness. In the analysis the bar is free to move radially outward under a centrifugal load, therefore relying on the laminations to support the full load of the bar. However, in reality the bar is clamped at each end ring, consequently supporting itself to an extent. Therefore the simulation can be seen as conservative.

The critical results are the maximum Von Mises stress equivalent illustrated in Figure 3-36, for the maximum interference and the CP shown in Figure 3-37 for the minimum interference. The simulation is done for a maximum operating speed of 19 000 r/min and a maximum operating temperature differential of 60 °C. Figure 3-36 shows the maximum stress is marginally above the allowed 225 MPa and has a FOS of 1.95 and this is deemed acceptable for the sub assembly. Figure 3-37 illustrates that the rod will put a large CP load on the tip of the bar slot, however, the results show that the laminations will not lose contact at the shaft interface.

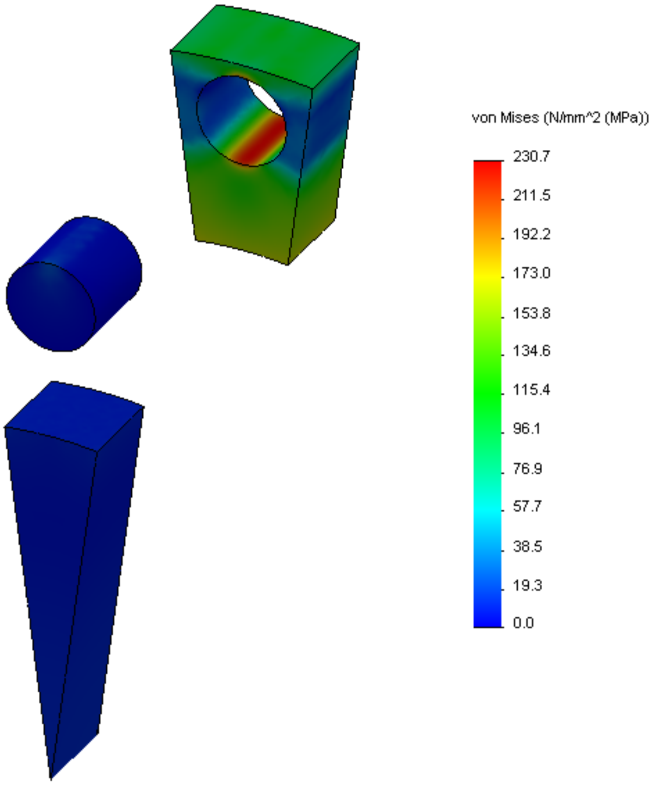

Figure 3-36: Shaft, lamination and conductive bar assembly, Von Mises stress

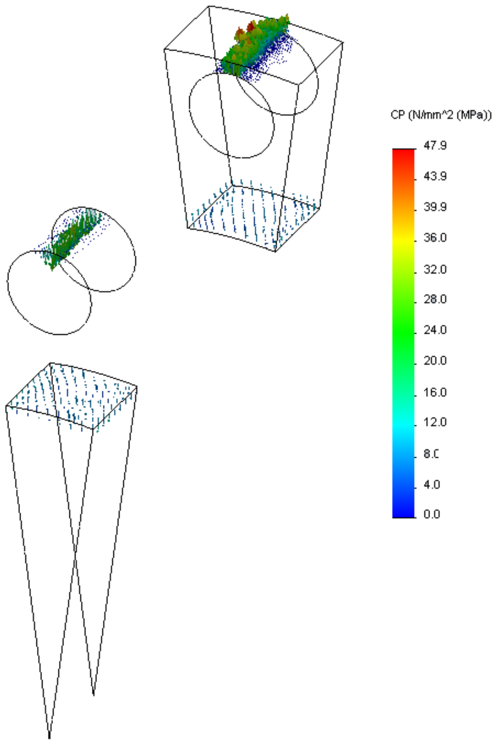

Figure 3-37: Shaft, lamination and conductive bar assembly, contact pressure

Table 3-13 is a summary of the CP at the shaft/laminations interface. The results show that for the minimum interference the average CP is 5.79 MPa. Consequently the results indicate that with the minimum interference the laminations will stay in contact at the maximum operating conditions.

Table 3-13: Summary of the CP at the shaft/laminations interface

	Max interference	**Min interference**
Average contact pressure (MPa)	8.62	5.79
Max contact pressure (MPa)	14.65	11.22
Min contact pressure (MPa)	4.83	3.28

3.7.4 Detail spacer stress analysis

Due to the current design specifications the rotor must be able to operate at an elevated temperature. The specifications allow for a 60 °C temperature increase. The complete IM rotor section is, however, assumed to have no temperature gradient. This can be seen as an accurate assumption due to the relative good conductivity of the materials used and a conservative estimation of the rise in temperature.

Consequently due to the difference in the thermal expansion coefficients of the conductive bars and magnetic core, the radial as well as the axial expansion of the components will be different. The effect of the relative expansion is illustrated in Figure 2-16 and Figure 2-17 and it is shown that a spacer with an oversize bar slot will reduce the effect. The spacer as illustrated in Figure 3-35 is purely a component which creates space, to allow the bar to be in bending and not shear. The ideal material would be Inconel 718 due to the low permeability, however, the budget did not allow this. Consequently it was decided to use the shaft material for the spacers as well. This was not ideal from an electromagnetic point of view. Furthermore the spacer is also used to clamp the lamination stack in order to machine and assemble it. The function of the spacer in terms of assembly will be discussed in detail during the manufacturing and assembly procedures in Chapter 4. The thickness of the spacer was dependent on the axial space required and the stiffness required for effective clamping. Because the spacers are to be used to clamp the lamination stack for manufacturing, the ID of the spacers and laminations will be the same. After numerous stress analyses the thickness of the spacer was chosen to be 4 mm. The detail drawings are included in **Error! Reference source not found.**.

This section shows the maximum Von Mises stress and CP due to the interference fit. The effect of the spacer will only be apparent in the full assembly simulations shown in section 3.7.8. Figure 3-38 illustrates the Von Mises stress fringe plot and shows a maximum stress of 261.9 MPa. Although the spacer and laminations have the same amount of interference the maximum stress is different. This is due to the larger bar slot in the spacer and the material has a higher modulus of elasticity (E) value. However, the maximum stress is much lower than the allowed maximum stress and the component has a FOS of about 2.7. Figure 3-39 shows the CP at the interface. The conductive bar is excluded from this stress analysis because it will not be in contact with the spacer and will have no effect on the maximum stress or CP in the shaft/spacer sub assembly.

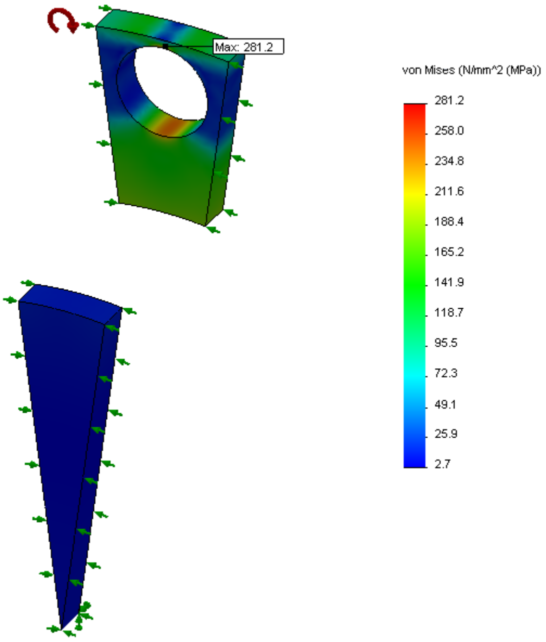

Figure 3-38: Shaft and spacer assembly, Von Mises stress

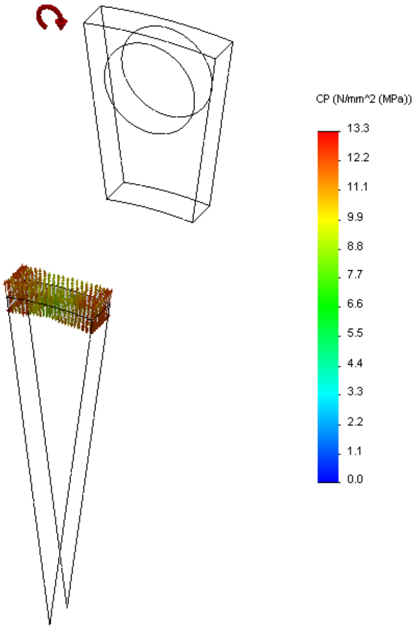

Figure 3-39: Shaft and spacer assembly, contact pressure

Table 3-14 is a summary of the CP at the shaft/spacer interface. The results show that for the minimum interference the average CP is 11.3 MPa. Consequently the results indicate that with the minimum interference the spacer will stay in contact at the maximum operating conditions.

Table 3-14: Summary of the CP at the shaft/spacer interface

	Max interference	**Min interference**
Average contact pressure (MPa)	14.4	11.3
Max contact pressure (MPa)	16.6	13.2
Min contact pressure (MPa)	12.2	9.2

3.7.5 Detail conductive bar stress analysis

From the literature it is apparent that most high speed IM rotors are designed with copper conductive bars and end rings. Apart from copper being an excellent electrical conductive material, it also allows the connection at the end ring/bar interface to be welded.

However, detail stress analysis show that the density of the conductive bars has a significant influences on the maximum stress found at the tip of the bar slot in the magnetic core, due to centrifugal forces. A increased bar density also results in an increased amount of interference required at the magnetic core/shaft interface. The increased amount of interference will in turn result, in an increase in maximum stress. Due to the limiting strength of the M270-35A lamination material selected, aluminium is the preferred bar material and although aluminium has a lower electrical conductivity compared to copper. The increase in resistivity can be reduced to an extent, by increasing the cross sectional area of the bar. The argument clearly shows that the choice in bar material is a compromise between the electromagnetic and mechanical designs and it was decided that the increase in rotational speed is worth the reduction in electrical efficiency.

The strength requirement of the conductive bar is significantly decreased by the implementation of the spacer. Due to this design feature the bar is subjected to compression, because of the thermal expansion, the compression stress is calculated to be 48.3 MPa. The connection type at the end ring conductive bar interface also contributes to the stress present in the bar. Initial calculations indicate that an relatively low strength aluminium can be used, however, aluminium 2024-T3 was available in 12 mm rod and for an increased FOS it was selected.

With the selection of aluminium 7075-T6 as the end ring material, the option of welding the end ring/bar connection is disqualified. Aluminium 7075-T6 cannot be welded without changing the material properties and due to the different materials used in the assembly, no heat treatments can be done afterwards to reverse the effects. Therefore an alternative connection is required which also considers the electrical contact resistance at the interface.

A few concepts were investigated, mainly bolted or interference fit connections, similar to those illustrated in section 2.3.3. During the evaluation of the concepts, the assembly of the squirrel cage was considered and was a critical parameter in the final selection. Different end ring/bar connection methods were selected for the two sides of the squirrel cage, mainly due to the assembly process. This is discussed in detail in Chapter 4 . The one side is a normal parallel interference fit and the other side has a small dowel pin forced into an undersized hole in the rod to create an interference connection at the end ring/bar interface.

Although chapter 4 is dedicated to the detail description of the entire induction machine (IM) rotor section, an overview of the squirrel cage assembly is required. Due to the shrink fit used to connect the IM rotor section to the shaft, a large temperature differential is required. Because of the difference in thermal expansion coefficients between the lamination stack and the conductive bars, the bars cannot be fixed at both ends. In order to limit the stress in the rotor section during assembly the one end of the bar is required to be free and expand axially. This implies that the connection at the one end ring is required after the assembly process is complete and the dowel pin is an elegant solution. The following sections present detail stress analysis of these two connections.

The amount of interference required for the parallel interference fit, utilized at the one end ring, is limited by the limiting strength of the end ring material. The stress in the end ring is a combination of the stress due to the end ring/shaft connection and the end ring/bar connection. After multiple FEM simulations the upper limit of interference at the bar/end ring interface is found. The results shown in Figure 3-40 is a FOS plot of the shaft end ring and bar assembly. The simulation is done for a speed of 19,000 r/min and no temperature differential, as this is the worst loading case. The results indicate for a maximum interference at the shaft/end ring interface, the end ring/bar interference should be limited to $\delta_d = 30\ \mu m$ to satisfy the FOS requirements.

On the other hand the electrical contact resistance at the interface should be minimized, resulting in a lower limit for the amount of interference. Due to the difficulty of calculating the electrical contact resistance, practical measurements are implemented to validate the design and are described later in the section.

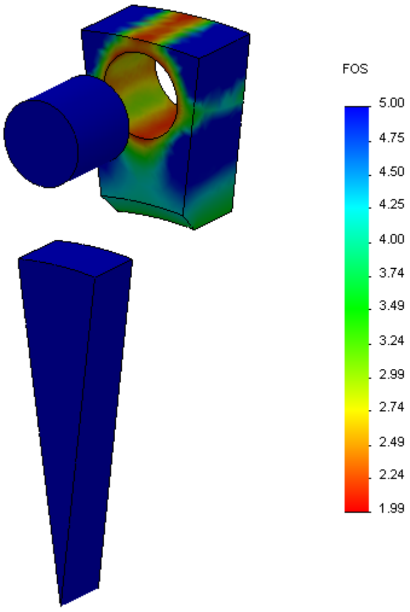

Figure 3-40: FOS plot of maximum shaft/end ring interference and 30 µm bar interference

The results show that the amount of interference at the bar/end ring interface due to the dowel pin, is also limited to 30 µm. Therefore the amount of interference at the dowel pin/bar interface is critical and is calculated in this section.

Due to the assembly process the bar slots in the one end ring and the bars will initially require a sliding fit. After the shrink fit of the IM rotor section a dowel pin is forced into the bar and the interference at the bar/end ring interface is created as illustrated in Figure 3-41. The bar's outer diameter is increased by forcing the 3 mm dowel pin into an undersized hole.

Figure 3-41: Schematic illustration of the interference fit produced by the dowel insert

In order to obtain any significant radial growth the amount of interference at the dowel pin/bar interface should be relatively large. First order analytical calculations are done using the Matlab® program. Figure 3-42 shows that for a radial interference at the dowel/bar interface of 50 µm, the bar

OD will increase with about 36 µm. However, calculating the Von Mises stress equivalent as indicate in Figure 3-43, it is seen that the bar material at the interface is above its yield strength. The dashed line indicates the yield strength of the materials and the solid line represents the calculated Von Mises stress due to the interference. The results show that the bar material will permanently yield up to a radius of 4mm. Indicating that the radial growth as calculated using the analytical model will be incorrect. The analytical model assumes that the material's elasticity is always linear and this is not correct, if the material is stressed above its yield strength, which it clearly is. The permanent deformation at the dowel/bar interface will reduce the effective interference, resulting in a decreased radial growth, possibly lowering the diameter growth below the maximum of 30 µm.

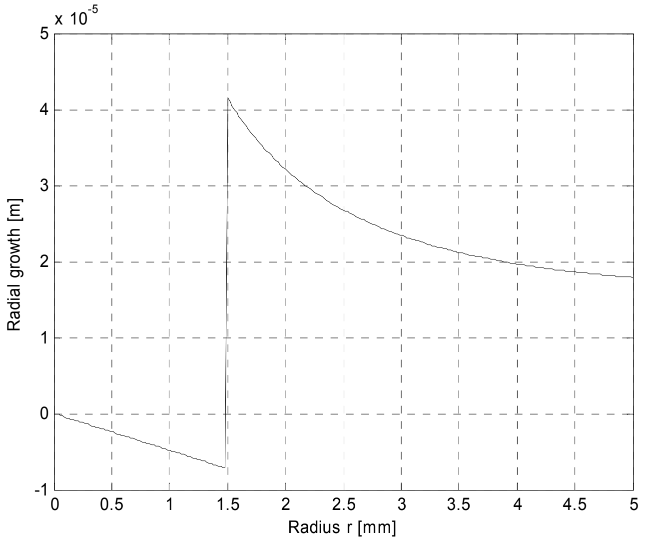

Figure 3-42: Analytically calculated bar radial growth

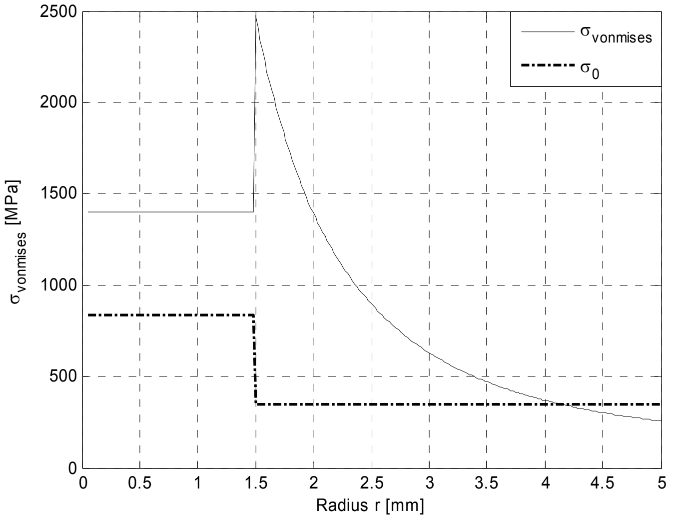

Figure 3-43: Von Mises stress distribution in the dowel and bar assembly

From the observation it is clear that a non-linear material model is required for the radial growth calculations. Figure 3-44 illustrates the Von Mises stress for a non-linear material FEM, the results also indicate that only the section close to the dowel will permanently deform. The simulation shows that the maximum stress is at the material's yield strength of 344 MPa and not 2500 MPa as shown in the analytical calculations. The simulation also indicates a reduced radial growth compared to the analytical calculations. In order to validate the radial growth, test samples are manufactured and the radial growth is measured.

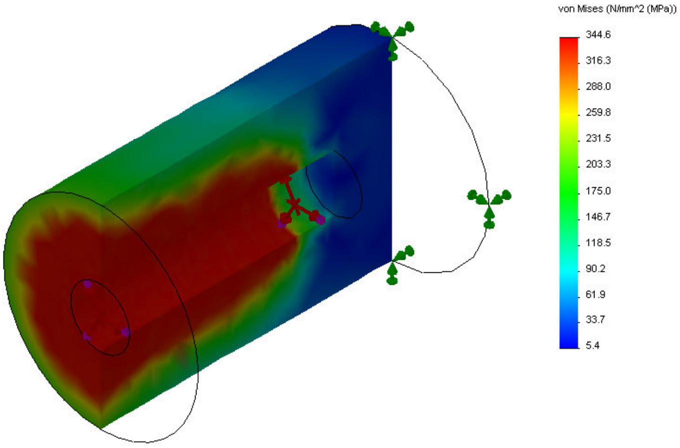

Figure 3-44: Section view of the Non-linear material FEM model for the dowel/bar interference fit

Figure 3-45 illustrates the bar test samples used in for the validation. The measurements are only applicable to the section where the dowel is inserted. Therefore, the samples are only a section of the bar as used in the IM. The picture shows a dowel pin, a bar with the hole, a bar and dowel pin assembled as well as the same assembly with a strain gage installed. The strain gage is used to measure the tangential strain and the increase in diameter can be calculated from the measurement. The measurements can also be done using a micrometer, however, the strain gage measurements is much more accurate and reliable.

Figure 3-45: Illustration of the bar test samples

Table 3-15 shows the calculated and measured results for the diameter growth after the dowel pin is inserted. Four strain gages were installed onto the four bar test specimens, two at 2.5 mm from the front as indicated in Figure 3-45. With the remaining two at 5 mm from the front, this was done to investigate the stress distribution. The results indicate that the diameter growth is not constant and shows a decrease in growth when moving further from the front. The measured growth also shows a good correlation to the FEM calculated growth.

Table 3-15: Conductive bar diameter growth calculations and test measurements

Specimen	Position from front (mm)	Voltage measurement (V)	Stress measured (MPa)	Measured Diameter growth (µm)	FEM diameter growth (µm)	Analytic diameter growth (µm)
1	5	2.86	125.20	17.16	22.06	35.76
2	5	2.96	129.85	17.80	22.06	35.76
3	2.5	4.62	202.53	27.76	27.54	35.76
4	2.5	5.37	235.58	32.29	27.54	35.76

The two strain gages installed at 5 mm from the front measures almost exactly the same diameter growth. The measurement also shows a good correlation with the FEM calculated growth. The gages installed 2.5 mm from the front indicate a difference in growth. However, the one measurement shows a good correlation with the FEM calculated growth. The reason for the difference in measurement was due to the installation method and it was found that the dowel angle as it is forced into the bar is critical. If the dowel is not perpendicular to the face of the bar-end the measurement is influenced significantly. From these measurements it is found what the maximum and minimum diameter growth will be and the end ring/bar interference fit stress calculations can be done using these results. After the connection type is selected and the amount of interference is validated the contact resistance at the interface can be measured and is discussed in the following section.

3.7.6 Validating end ring/bar connection electrical contact resistance

The squirrel cage is made of a low resistive material and any increase in resistance will influence the efficiency of the IM. The contact resistance at the end ring/bar interface is critical and should be minimised. To investigate the effect of the interference fit, a test setup as illustrated in Figure 3-46 is used [50]. Figure 3-46 shows the end ring/bar assembly with a 5 µm radial interference at the interface. The test setup also includes a battery and probes used to measure the contact resistance. A 12 V battery is used as the power supply and a shunt is coupled in series with the end ring/bar assembly. The voltage drop across the shunt is measured and with its resistance known the current is be calculated. The voltage drop across the end ring/bar interface is also measured and with the current known the contact resistance is be calculated.

Table 3-16 shows the results obtained from the test measurements. The results indicate a measured contact resistance of between 6.16 and 9.16 µΩ. The measured resistance is relatively low compared to the resistance of the bar which can be calculated to be 1.149 mΩ. A simple calculation indicates that the contact resistance is more than 125 times less than the conductive bar’s resistance. Therefore the contact resistance can be neglected and the connection type, can be assumed to be sufficient at only a radial interference of 5 µm.

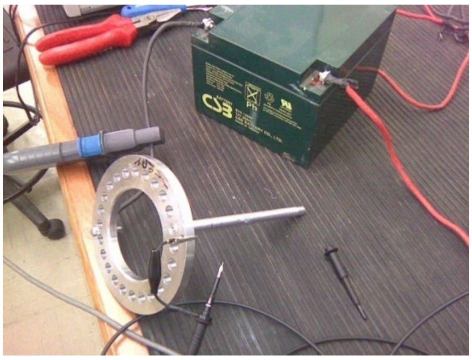

Figure 3-46: End ring/bar interface contact resistance measurement setup

Table 3-16: Contact resistance measurements

Test number	Voltage across shunt (V)	Current (A)	Voltage across contact (V)	Contact resistance (Ω)
1	1.340	893.3	6.00E-03	6.716E-06
2	1.315	876.6	5.40E-03	6.160E-06
3	1.310	873.3	8.00E-03	9.160E-06
4	1.320	880.0	8.00E-03	9.091E-06

The electrical contact resistance measurements indicate that contact resistance is negligible and will not influence the IM's electrical efficiency significantly. These results confirms that a interference fit with only a 10 µm diameter interference will be sufficient as the bar/end ring connection. The fact that the amount of interference will be the same at 0 r/min and 19,000 r/min suggests that the contact resistance will stay the same and is not dependent on rotational speed.

The strain gage measurements of the diameter growth indicate a maximum growth of 32 µm. The amount of interference can now be used to calculate the stress in the end ring due to the end ring/shaft connection as well as the end ring/bar connection and is discussed in detail in the following section.

3.7.7 Detail end ring stress analysis

Using the results from the measured radial growth of the bar due to the dowel insert and the end ring/shaft connection, the maximum stress in the end ring can be calculated. The initial calculations indicate that the end ring will require an increased interference compared to the spacer and laminations, mainly due to the lower modulus of elasticity of the aluminium. Due to the increased interference, the end rings' ID cannot be machined with the spacers and lamination stack. This also influences the assembly of the rotor and the concentricity alignment becomes critical, as will be discussed in Chapter 4.

The maximum end ring stress calculations are done for the maximum end ring/shaft interference which is $\delta_d \approx 156$ µm and maximum end ring/bar interference. The maximum interference at the end ring/bar interface is calculated using the measured diameter growth of the bar and calculating the allowable dimensional tolerance of the bar slot. The actual measured maximum diameter growth of the bar is 32 µm and the maximum allowable bar/end ring interference is calculated to be 30 µm as shown in section 3.7.5. Selecting to manufacture all of the bar slots to the same diameter, implies that the conductive bar's two ends will require two different initial diameters as illustrated in Table 3-17.

Table 3-17: Conductive bar and slot dimensions

Component	**Max dimension (mm)**	**Min dimension (mm)**	**Interference (µm)**
Conductive bar slots	10.005	10.000	N/A
Conductive bar dowel	10.030[11]	10.020	24
Conductive bar parallel fit	10.030	10.010	14

The resulting maximum interference at the bar/end ring interface is the maximum bar diameter of 10.030 mm minus the minimum slot size of 10.000, resulting in an interference of $\delta_d \approx 30$ µm. The results indicate that the worst loading scenario is at maximum operating speed and room temperature. The reason the maximum stress is lower at higher operating temperature is due to the higher thermal expansion coefficient of the Aluminium end ring. As the operating temperature increases the amount of interference is reduced, resulting in a reduction in stress in the end ring.

Figure 3-47 shows the maximum Von Mises stress distribution for the shaft, end ring and conductive bar assembly. The bar is a simplified model that does not incorporate the dowel pin, however, the bar is modelled with the appropriate interference. The maximum stress calculated translates to a FOS of 2.03

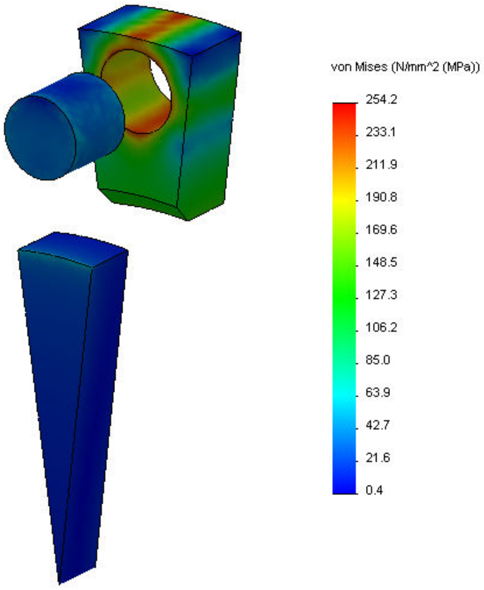

Figure 3-47: Von Mises stress distribution of the shaft, end ring and bar assembly

---

[11] Initial OD of the bar is 9.995 mm. After the insertion of the dowel the OD increased by a maximum of 35 µm.

The contact pressure calculated from the minimum interference and maximum operating speed and temperature, which is the worst loading scenario, shows that the end-ring loses contact with the shaft. However, the simulation of the entire IM rotor section, discussed in the following section, shows that the end ring will not lose contact with the shaft at these operating conditions. This is due to the difference in constraints between the shaft/end ring sub-assembly and complete IM rotor section simulation. In the complete model there is a no-penetrating connection with friction between the end ring, spacer and shaft shoulder which in the individual simulation cannot be simulated correctly. The laminations also support the conductive bar and therefore, limiting the end ring's radial displacement.

3.7.8 Detail stress analysis of the complete IM rotor section

After simulating the individual sub-assemblies, insight in the reaction of the components under loading conditions is obtained. The calculations also gave an indication of the amount of interference required. However, in order to evaluate the integrated effect of the loading conditions the complete IM rotor section is evaluated.

Figure 3-48 illustrates an exaggerated displacement side view of the complete assembly under maximum operating speed and temperature. The result gives insight into how the rotor reacts under these loading conditions. The relative growth between the magnetic core and the conductive bar can clearly be seen and how that effects the end ring's displacement.

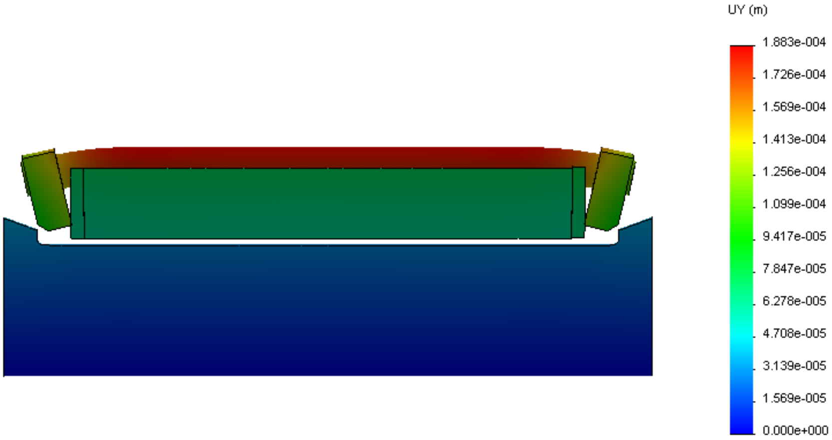

Figure 3-48: Exaggerated displacement of the complete IM rotor section under load

In order to verify the FEM results of the complete assembly, the results are compared to those of the sub-assemblies. Consequently, simulations of the complete assembly for both the maximum and minimum interference is required.

Furthermore, the critical parameter for the maximum interference is the maximum stress, Figure 3-49 shows the FOS plot of the maximum interference assembly. The minimum FOS is calculated to be 1.88, however, the areas where the FOS is below 2 are barely visible. The stress results from this simulation are compared to the results from the sub-assemblies presented earlier and are summarised in Table 3-18. The results compare the maximum stress in the shaft/laminations, shaft/spacer and shaft/end ring sub-assemblies to the corresponding components in the complete assembly. The stress due to the bar/end ring interference forms part of the shaft end ring sub-assembly and contributes to the stress in that sub-assembly. The results indicate a good correlation between the simulations, with a maximum variation of 2.2 % for the shaft/end ring comparison.

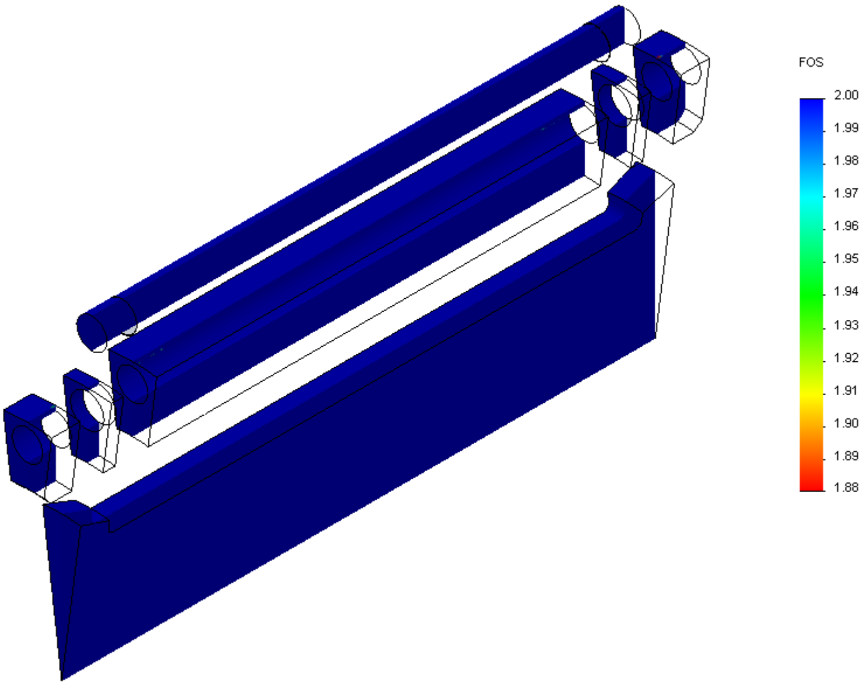

Figure 3-49: FOS plot for complete IM rotor section maximum interferences

Table 3-18: Comparison of Von Mises stress for maximum interference of the sub- and complete assembly

Shaft/Laminations			
	Sub-assembly	**Complete assembly**	**Variation (%)**
Max Von Mises stress (MPa)	230.3	233	**1.3**
Shaft/Spacer			
	Sub-assembly	**Complete assembly**	
Max Von Mises stress (MPa)	281.2	286.2	**1.7**
Shaft/End ring/Conductive bar			
	Sub-assembly	**Complete assembly**	
Max Von Mises stress (MPa)	254.2	260	**2.2**

The critical parameter for the minimum interference simulation is the CP at the interfaces of each shrink fitted component. The average CP for the sub-assemblies is compared to the CP of the individual components found from the complete assembly simulation results as presented in Figure 3-50. The results summarised in Table 3-19 indicate that the average CP for all the components is higher in the complete assembly when compared to the sub-assemblies results. The increased CP is a result of the interaction between the components in the complete assembly, due to friction at the interfaces. This also explains the increased CP at the shaft/end ring interface as discussed in the detail stress analysis of the shaft/end ring sub-assembly in section 3.7.7.

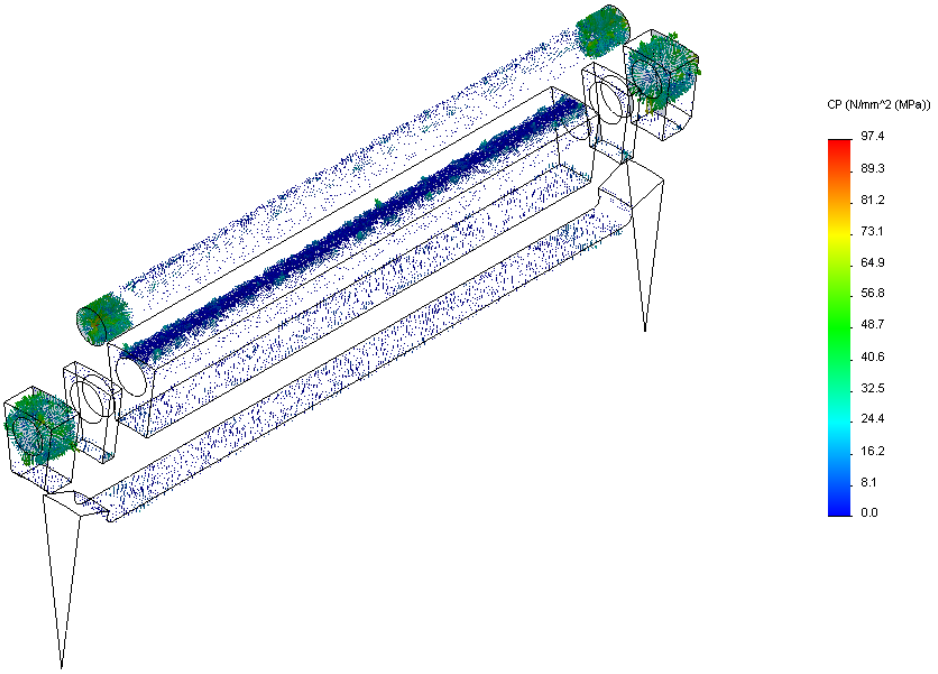

Figure 3-50: Calculated CP for complete IM rotor section with minimum interferences

Table 3-19: Comparison of CP stress for minimum interference for the sub- and complete assembly

Shaft/Laminations			
	Sub-assembly	**Complete assembly**	**Variation (%)**
Average CP (MPa)	5.79	6.16	**6.0**
Shaft/Spacer			
	Sub-assembly	**Complete assembly**	
Average CP (MPa)	11.3	12.64	**10.6**
Shaft/End ring/Conductive bar			
	Sub-assembly	**Complete assembly**	
Average CP (MPa)	-	5.03	**N/A**

From the machines power (75 kW) and speed rating (19,000 r/min) the maximum torque to transfer (M_t) is calculated to be 37.71 Nm. Implementing (3.4) the minimum contact pressure (p_c) at the IM rotor section/shaft interface required, before any slip at the interface occurs, is calculated. Assuming for a worst case scenario that only the lamination stack should transfer the entire torque load of 50.26 Nm, the parameters required to calculate the minimum contact pressure is. Interface diameter (d_c = 0.08 m), axial length of contact area (l = 0.15 m) and the friction coefficient μ for shrink fits is given as 0.125 [51]. The result indicate that minimum contact pressure of 128,1 kPa is required, which is much less than the expected 6.16 MPa. Therefore the calculation show that the minimum amount of interference is more than enough to transfer the maximum expected torque.

$$M_t = \frac{\pi d_c^2 l \mu p_c}{2} \tag{3.4}$$

Although the results indicate that the rotor can be safely operated at 19,000 r/min and 80°C it is very much dependent on the final dimensions of all the components. Therefore, the critical dimensions of each component are measured after final manufacturing. The measuring is done in a temperature controlled facility at Denel Dynamics Pty Ltd using a high precision 3D measuring device and is presented in chapter 4.

3.8 Conclusion

In conclusion, during the mechanical design chapter the iterative design process was discussed and the process was implemented in order to obtain a solution for the current design problem. The mechanical design was started through the introduction of analytical equations which can be used to calculate preliminary maximum stresses in an IM rotor section. However, upon investigation (3.1) proved to be ambiguous and a modification factor, which is dependent on material properties, was proposed. The preliminary stress calculations were useful to obtain an idea of the required material yield strength.

After preliminary material selection, Larsonneur's two ring interference fit derivation was used to calculate first iteration interference fit requirement. Although Larsonneur's analytical model does not allow for stress concentrations, the amount of interference calculated can be used as a first iteration value. However, to compensate for the stress due to the bar slot, stress concentration factors (K_t) were investigated. Paterson presents a stress concentration graph that can be used to find the K_t for specific parameters. However, due to the specific geometry, extrapolation of the K_t value was required, putting the integrity of the K_t at stake.

After systematically verifying and validating the FEM in terms of loads, constraint, mesh size and symmetry function, the model was used to verify the analytical K_t value. The results showed a significant discrepancy. Upon further investigation, using a test setup and measuring the actual stress at the stress concentration position, it became evident that the Paterson's K_t value is conservative for this particular geometry and the FEM is correct.

Due to the systematic breakdown of the sub-assembly-FEM models, the results were proven to be correct. When these results are compared to the results from the complete assembly the results indicate a good correlation and the complete assembly's results can be assumed correct.